Upgrade of the IMD software tool for the simulation of laser-matter interaction

Upgrade des Programms IMD zur Simulation von Laser-Materie Wechselwirkung
Master-Thesis von Marco Patrizio
Tag der Einreichung:

1. Gutachten: Professor Dr. Markus Roth
2. Gutachten: PD Dr. Johannes Roth

TECHNISCHE
UNIVERSITÄT
DARMSTADT

Fachbereich 5 - Physik

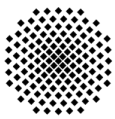

University of Stuttgart
Germany

Deutsches Zentrum
für Luft- und Raumfahrt
German Aerospace Center

Upgrade of the IMD software tool for the simulation of laser-matter interaction
Upgrade des Programms IMD zur Simulation von Laser-Materie Wechselwirkung

Vorgelegte Master-Thesis von Marco Patrizio

1. Gutachten: Professor Dr. Markus Roth
2. Gutachten: PD Dr. Johannes Roth

Tag der Einreichung:

Erklärung zur Master-Thesis

Hiermit versichere ich, die vorliegende Master-Thesis ohne Hilfe Dritter nur mit den angegebenen Quellen und Hilfsmitteln angefertigt zu haben. Alle Stellen, die aus Quellen entnommen wurden, sind als solche kenntlich gemacht. Diese Arbeit hat in gleicher oder ähnlicher Form noch keiner Prüfungsbehörde vorgelegen.

Darmstadt, den September 28, 2015

(Marco Patrizio)

Abstract

The simulation of the laser ablation processes can be a valuable tool for studying coupling parameters and developing questions for future experiments. The theory behind the ablation process and the mathematical model to describe laser beam absorption are discussed. Further, the simulation tools IMD and Polly-2T, used at the Institute of Technical Physics, DLR Stuttgart, are introduced and a road map for the upgrade of IMD is proposed. This upgrade is aimed towards including a more advanced physics model present in Polly-2T into IMD, to enhance the validity of the laser absorption process for laser pulses beyond the femtosecond regime. This is achieved by implementing the target reflectivity according to the Fresnel formulas and dynamic calculation of the permittivity following a wide-range approximation of the permittivity for different material states. The wide-range approximation is also implemented for the electron thermal conductivity and the electron-phonon coupling. The implementation of critical upgrade steps in IMD is presented and the results are compared to Polly-2T. Persistent issues and bugs of the upgrade are discussed and possible solutions for future improvements and further upgrades are outlined.

Contents

1 Motivation **9**

2 Theory **11**
2.1 Laser . . . 11
2.1.1 Spontaneous and Stimulated Emission . . . 11
2.1.2 Absorption . . . 12
2.1.3 Coherent Light Amplification . . . 13
2.1.4 Population Inversion . . . 13
2.2 Laser-Matter Interaction . . . 14
2.2.1 Light Propagation . . . 14
2.2.2 Laser Ablation . . . 17
2.3 Two Temperature Model . . . 18
2.3.1 Femtosecond Pulse . . . 19
2.3.2 Picosecond Pulse . . . 20

3 Software Details **21**
3.1 Molecular Dynamics and IMD . . . 21
3.1.1 Molecular Dynamics - Basics . . . 21
3.1.2 Two Temperature Model in IMD . . . 23
3.1.3 Transport Properties . . . 24
3.1.4 Optical Properties . . . 24
3.2 Hydrodynamics and Polly-2T . . . 25
3.2.1 Governing Equations . . . 25
3.2.2 Two Temperature Model in Polly-2T . . . 25
3.2.3 Transport Properties . . . 25
3.2.4 Optical Properties . . . 27
3.3 Summary - Comparison of IMD and Polly-2T . . . 29

4 Approach for an Upgrade of IMD **31**
4.1 Cold Reflectivity . . . 31
4.2 Dynamically Changing Reflectivity . . . 32
4.3 Temperature-dependent Energy Absorption . . . 32
4.4 Optional Goal . . . 32

5 IMD Bugs **34**

6 Results **36**
6.1 Cold Reflectivity . . . 36
6.1.1 IMD Upgrades . . . 36
6.1.2 Polly-2T Downgrades . . . 37
6.1.3 Parameter File Generator . . . 37

6.1.4 Simulation . . . 37
6.1.5 Data Analysis . . . 38
6.1.6 Conclusion . . . 41
6.2 Dynamic Reflectivity . . . 42
6.2.1 IMD Upgrade . . . 42
6.2.2 Simulation . . . 42
6.2.3 Data Analysis . . . 44
6.2.4 Conclusion . . . 44
6.3 Temperature-Dependent Energy Absorption . . . 46
6.3.1 Upgraded Energy Absorption Scheme . . . 46
6.3.2 Implementation of the Wide-Range Model for ϵ . . . 48
6.3.3 Further Changes to IMD . . . 48
6.3.4 Known Issues . . . 49
6.3.5 Simulation . . . 50
6.3.6 Data Analysis . . . 50
6.3.7 Conclusion . . . 54
6.4 Wide-range model for κ_e and γ_{ei} in IMD . . . 55
6.4.1 Implementation . . . 55
6.4.2 Simulation . . . 55
6.4.3 Data Analysis . . . 55
6.4.4 Conclusion . . . 57

7 Discussion **58**

8 Summary and Outlook **62**

9 Acknowledgement **63**

10 Appendix **65**

Nomenclature

EAM	Embedded Atom Model
EM	electromagnetic
EOS	Equation of State
FD	finite difference
HD	hydrodynamics
IMD	ITAP Molecular Dynamics
IMDu	IMD unit
MD	molecular dynamics
TTM	Two Temperature Model
$\hbar = h/2\pi$	Planck's constant / 2π
$c = 2.99792458 \cdot 10^{8}\ m/s$	Speed of light in vacuum
$e = 1.60217657 \cdot 10^{-19}\ C$	Electron charge
$h = 6.62606957 \cdot 10^{-34}$ kg m^2/s	Planck's constant
$k_B = 1.3806488 \cdot 10^{-23}\ J/K$	Boltzmann's constant
α	Optical absorption coefficient
χ_{FD}	Minimum thickness of one FD cell
ϵ	Absolute permittivity in complex representation
ϵ_{bb}	Permittivity from band to band interactions
ϵ_{met}	Permittivity in the metal phase
ϵ_{pl}	Permittivity in the plasma phase
γ	Linear scaling factor
$\Gamma_{\text{e-ph}}$	Coupling coefficient between electron and ion subsystem (basic TTM)
γ_{ei}	Coupling parameter for electron-ion coupling (Polly-2T)
κ	Thermal conductivity
κ_e	Electron thermal conductivity
κ_e	Thermal conductivity of the electron subsystem

κ_i	Thermal conductivity of the ion subsystem
λ	Wavelength
$\mathbf{E}$	Electrical field
$\mathbf{F}$	Force vector
$\mathbf{p}$	Impulse vector
$\mathbf{r}$	Spatial vector
$\mathbf{v}$	Velocity vector
$\mathbf{v}^T$	Thermal velocity
$\mathbf{v}_{CM}$	Center of mass velocity
μ_r	Relative permeability
ν	Frequency of an electromagnetic wave
$\nu_{\text{eff,p}}$	Effective collision frequency
$\nu_{\text{max,p}}$	Maximum collision frequency
$\nu_{\text{met,p}}$	Collision frequency in the metal phase
ν_{pl}	Plasma frequency
ω_L	Laser frequency
Φ	Core-core potential
Φ_{abs}	Absorbed fluence
Φ_{laser}	Output fluence of the laser
Φ_{surf}	Surface fluence
Φ_a	Absorbed fluence
Φ_a^{min}	Minimum absorbed fluence required for ablation
ρ	Density
ρ	Local electron density
$\sigma \equiv \sigma_{21} = \sigma_{12}$	Transition cross section
τ	Pulse length of the laser beam
τ_l	Pulse length of the laser beam
τ_s	Spontaneous emission lifetime
$\tau_e = C_e/\Gamma_{\text{e-ph}}$	Coupling time of the electron subsystem to the ion subsystem

$\tau_{ph} = C_i/\Gamma_{\text{e-ph}}$	Coupling time of the ion subsystem to the electron subsystem
θ	Incidence angle
ξ	Modified coupling parameter for electron-ion coupling (IMD)
A	Area
B	Single component magnetic field envelope
C_e	Heat capacity of the electron subsystem
C_i	Heat capacity of the ion subsystem
c_p	Specific heat capacity
E	Energy
E	Single component electrical field envelope
E_{0i}	Incident energy
E_{0r}	Reflected energy
E_{0t}	Transmitted energy
F	Electron hull-core potential
$F = I/(h\nu)$	Photon flux
H	Enthalpy
H^a	Enthalpy required for ablation
H_ν	Enthalpy of evaporation at the boiling temperature of the solid
H_s	Total enthalpy of the material
I	Intensity
J_i	Material flux
l	Length
l_α	Absorption depth of the laser beam
l_e	Diffusion length of heated electrons
$m_e = 9.10938 \cdot 10^{-31}\ kg$	Electron mass
N	Number of particles
n	Complex refraction number

N^e	Number of particles at thermal equilibrium
n_e	Electron concentration
N_s	Atom number density
n_{cr}	Critical electron concentration
P_e	Electron pressure
P_i	Ion pressure
Q	Source term for laser heating
Q_L	Source term for laser absorption
S_s	Total surface energy flux
T	Temperature
t	Time
T_0	Initial temperature
$T_{\text{el,max}}$	Maximum electron temperature
T_e	Temperature of the electron subsystem
T_F	Fermi temperature
T_i	Temperature of the ion subsystem
T_s	Surface Temperature
T_{st}	Stationary Temperature during ablation
u	One dimensional velocity
V	Material specific volume
V	Potential
v	Velocity
W_{21}	Rate of stimulated emission
x, y, z	Directional denominators according to euclidean coordinates
Z	Mean charge of the ions

1 Motivation

Astronomy and cosmology search for more and more precise instruments to fathom the nature of our universe. To achieve these goals future instruments include new space-born detection and observation systems [1] that require highly precise means of attitude and orbital control. Microthrust engines with thrust values in the range of μN to mN might be able to fulfil this role [2]. One possible realisation of such a microthrust engine is the laser-ablative microthruster, featuring a high specific impulse and long lifetime compared to the more common chemical thrusters. Following Arthur Kantrowitz's "4-P Principle"(Payload, Propellant, Photons, Period)(as referred to in [2]) the Institute of Technical Physics (DLR Stuttgart) is researching the possibility of an inertia free laser-ablative microthruster, that negates interferences to the thrust vector and vibrations by omitting moving parts in the design.
The definition of a laser engine is an "engine, in which laser energy contributes a substantial and indispensable part to the kinetic energy" [3]. The laser-ablative micro thruster generates thrust by introducing laser energy into a fuel material, such that a material specific threshold is exceeded and ablation of the materials surface layers can occur. The recoil from the ejected material generates the thrust for this kind of engine. Laser-ablative thrusters can regulate their

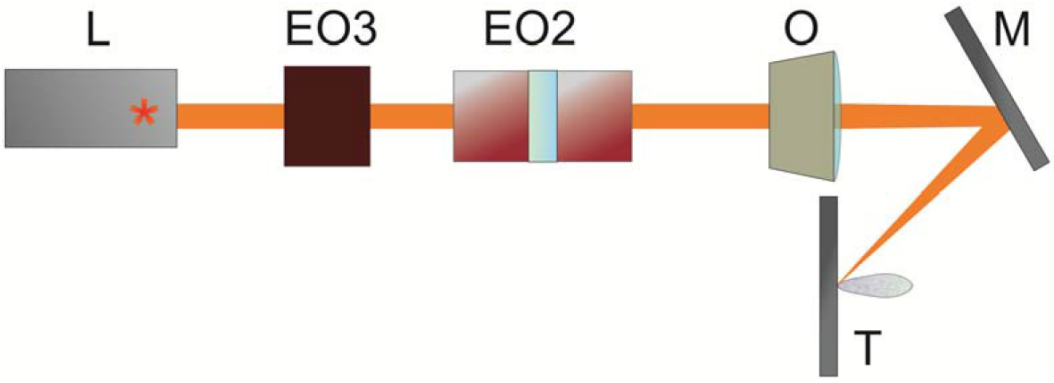

Figure 1.1: Concept of the laser-ablative micro thruster consisting of a pulsed microchip laser (L), an electro-optical lense (EO3), an electro-optical beam steering device (EO2), an optical lens with a fixed focus length (O), a plane mirror (M) and a metallic target (T). [2]

thrust by changing the repetition rate of their pulsed laser, increasing or decreasing the amount of ablated material in a certain time interval. Our concept is founded on the idea that even after several scans over the surface of the propellent block, the thrust per laser pulse stays the same. To validate this hypothesis, simulations of the ablation process and surface cratering are required.
The Institute of Technical Physics uses two different software tools for these simulations, the ITAP Molecular Dynamics code (IMD) developed at the Institute of Theoretical and Applied Physics, University of Stuttgart and the Polly-2T code by the Joint Institute for High Temperatures at the Russian Academy of Sciences in Moscow. While both simulation tools use the Two Temperature Model as a basis for the material heating by the laser, their underlying framework is quite different. IMD is based on molecular dynamics, while Polly-2T is a hydrodynamic code,

Polly-2T also uses a more advanced physics model for energy absorption and transport. The findings in [4] show that for laser pulses in the fs-range and low laser fluences, IMD and Polly-2T yield comparable results, while at greater pulse lengths and/or higher fluences the results start to differ. Upgrading the implementation of the energy absorption and the two temperature model in IMD, in order to accommodate for changing material parameters during longer pulses and higher laser energy, might mitigate these differences.

2 Theory

The physical background behind laser-ablative micro thrusters is an overlap of different physical regimes, as the generation of the laser beam is governed by laser physics, the beam propagation and deflection by optical effects, while the ablation process can be described by material science and condensed matter physics. This chapter will give an introduction into the physical principles behind the aspects of laser ablation, while also focusing on the theory behind the two different types of simulation software used during this thesis. The theory about lasers can be found in [5], which serves as the basis for the following section.

2.1 Laser

A laser is a device that generates a high intensity beam of monochromatic light that is highly coherent and highly directional. The name "laser" is an acronym for *light amplification by stimulated emission of radiation*. The laser was developed as an extension of the maser (*Microwave amplification by stimulated emission of radiation*) to the optical and infra-red spectrum.
There are three components integral to the design of a laser.

- The gain medium that uses the process of *stimulated emission* to amplify the light. The gain medium can be a gas, a liquid or solid.
- The pump source that is used to create a *population inversion* in the gain medium to enable the amplification. A variety of systems can be used as pump sources, such as an electrical discharge or a flash lamp.
- The resonator, which often consists of a pair of mirrors that trap the light inside the resonator cavity. Where one mirror called the *output mirror* is semi-reflective and allows a fraction of the light inside the resonator to escape in form of the beam.

Two general groups of lasers exist, that differ in how their energy transmission develops over time. Continuous wave (CW) lasers generate an output beam that has little to no change in its temporal profile and delivers a beam with constant amplitude and frequency, while pulsed lasers transmit their energy in a short pulse and can usually be used in a repetitive fashion. Pulse durations for pulsed lasers are usually in the range of nanoseconds to femtoseconds (see [5]).

2.1.1 Spontaneous and Stimulated Emission

Absorption and emission of electromagnetic waves can be described in the model of two energy levels. We define E_1 as the energy of the ground state of the system and E_2 as the energy of an excited state. If the initial energy level is E_2, the system will spontaneously decay into the stable ground state while releasing a photon (see Fig. 2.1(a)) that carries the energy $\Delta E = E_2 - E_1$ and therefore the frequency

$$\nu = \frac{\Delta E}{h} \tag{2.1}$$

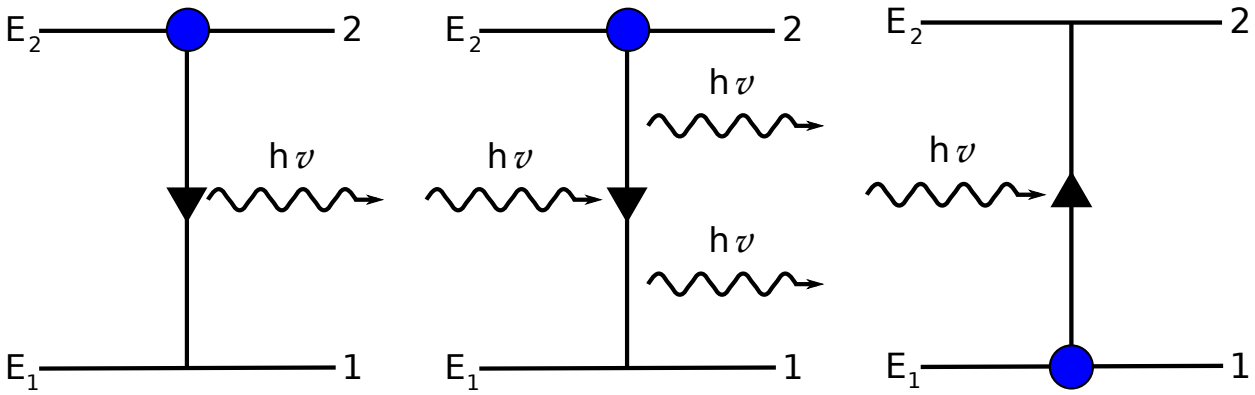

(a) Spontaneous emission (b) Stimulated emission (c) Absorption

Figure 2.1: Schematic of the emission and absorption processes for photons as shown in [5]

The emitted photon can be emitted in any direction with an arbitrary polarisation, resulting in unpolarised non-coherent light.
Since the decay to the ground state is governed by quantum mechanics one needs to consider an ensemble of systems (e.g. atoms, molecules) to gain knowledge about the characteristic time scale of this decay. If there are N_2 systems in the state E_2, the decay rate for spontaneous decay can be calculated according to [5] as

$$\left(\frac{dN_2}{dt}\right)_{sp} = -\frac{N_2}{\tau_s}. \tag{2.2}$$

If the system interacts with a photon with the frequency ν_i that is identical to the frequency of excitation between E_1 and E_2, the system has a probability to decay into its ground state while emitting a photon with the same frequency as the incident photon (see Fig. 2.1(b)) and will also adopt its direction, polarisation and phase. The rate of stimulated emission in an ensemble can be described by

$$\left(\frac{dN_2}{dt}\right)_{st} = -W_{21}N_2, \tag{2.3}$$

where the emission rate W_{21} is proportional to the flux of incoming photons.

2.1.2 Absorption

In the case of the system being in the ground state 1 and there are no interactions with the system, it will stay in the stable ground state. However, if there is an electromagnetic wave interacting with the system, that has a frequency corresponding to the energy difference between the ground state 1 and an excited state 2, there is a probability of the system absorbing the electromagnetic wave/photon and switching into its excited state (see Fig. 2.1(c)).

2.1.3 Coherent Light Amplification

Amplification of light intensity in the gain medium of a laser can be described as a feedback between *absorption* and *stimulated emission*. The change in photon flux dF in z-direction can be calculated as

$$dF = \sigma(N_2 - N_1)F(z)dz, \tag{2.4}$$

where σ is the cross section of absorbing and stimulated emission of photons.
If the number of systems in the excited state is larger than the number of systems in the ground state the medium will act as an *optical amplifier*, since more photons will be coherently emitted by stimulated emission than are absorbed, thus increasing the total photon flux. If the number of systems in the excited state is smaller than the number of photons in the ground state the medium will act as an absorber, since more photons will be absorbed than are emitted, thus decreasing the total photon flux.

2.1.4 Population Inversion

The case in which the number of systems in the excited state (N_2) is larger than the number of systems in the ground state (N_1) is called *population inversion*. However, comparing the population number at thermal equilibrium N^e in the Boltzmann statistics,

$$\frac{N_2^e}{N_1^e} = \exp\left(-\frac{E_2 - E_1}{k_B T}\right) \tag{2.5}$$

shows, that at thermal equilibrium the population numbers N_2^e is a lot smaller than N_1^e and therefore any material will behave as an absorber in thermal equilibrium. To achieve an optical amplification in the medium, as needed for a laser, the populations of N_2 and N_1 have to be inverted by means of *pumping*. Pumping can be done by irradiating the material with EM

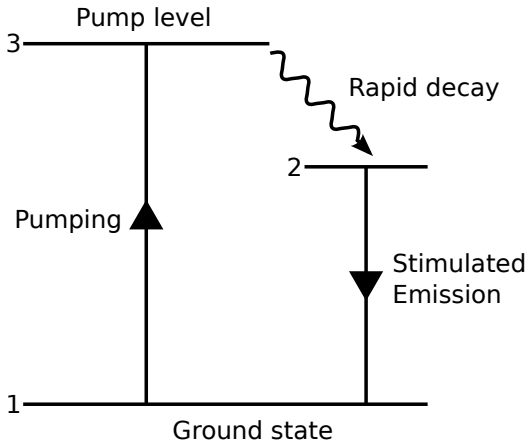

Figure 2.2: Schematic of a three-level pumping process

radiation of the frequency $\nu = E_2 - E_1$, due to the higher number of systems in the ground state, more of the radiation will be absorbed than is emitted by stimulated emission. However, the feedback between absorption and emission would prevent the occupation numbers of states 1

and 2 to achieve a population inversion, thus reaching an equilibrium between N_1 and N_2 at which the material becomes transparent for the frequency ν. To reach the population inversion at least one more energy level is required. As shown in Fig. 2.2 the pumping raises the system in a rapidly decaying excited state 3. From there it decays into a *semi-stable* state 2 with a longer life time than 3, therefore creating a population where $N_2 > N_1$, caused by the rapid decay of $3 \rightarrow 2$ compared to $2 \rightarrow 1$. Since 3 and 2 possess different energy levels the frequency used for pumping is different from the frequency causing stimulated emission from $2 \rightarrow 1$, thus avoiding feedback.

2.2 Laser-Matter Interaction

Laser matter interaction describes a wide field of effects, depending on the energy and pulse length of the incident laser beam. Since the focus of this thesis is on *laser ablation* and light propagation in material, the following section will describe the laws governing the light propagation and the process of ablation according to [6].

2.2.1 Light Propagation

Whenever a beam of light traverses the boundary between two media with different refraction values, the beam will be split into a reflected and a refracted beam, with the exception of the case of *total reflection*. The reflected beam will possess an exit angle equal to the incident angle, while the refracted angle can be described by *Snellius' law*, both cases are shown in Fig. 2.3,

$$n_1 \sin(\theta_1) = n_2 \sin(\theta_2), \tag{2.6}$$

where n_1 and n_2 are the refraction values of the media 1 and 2, while θ_1 and θ_2 are the angles of the beam in the respective media in reference to the plumb-line on the surface. With this equation the exit angle can be described with respect to the incidence angle and the refraction values.
To describe the portion of the incident beam energy that is allocated to the reflected and refracted beam respectively, the *Fresnel equations* can be used

$$\left(\frac{E_{0t}}{E_{0i}}\right)_S = \frac{2n_1 \cos(\theta)}{n_1 \cos(\theta) + \frac{\mu_{r1}}{\mu_{r2}}\sqrt{n_2^2 - n_1^2 \sin^2\theta}}, \tag{2.7}$$

$$\left(\frac{E_{0r}}{E_{0i}}\right)_S = \frac{n_1 \cos\theta - \frac{\mu_{r1}}{\mu_{r2}}\sqrt{n_2^2 - n_1^2 \sin^2\theta}}{n_1 \cos\theta + \frac{\mu_{r1}}{\mu_{r2}}\sqrt{n_2^2 - n_1^2 \sin^2\theta}}, \tag{2.8}$$

$$\left(\frac{E_{0t}}{E_{0i}}\right)_P = \frac{2n_1 n_2 \cos\theta}{n_2^2 \frac{\mu_{r1}}{\mu_{r2}} \cos\theta + n_1\sqrt{n_2^2 - n_1^2 \sin^2\theta}}, \tag{2.9}$$

$$\left(\frac{E_{0r}}{E_{0i}}\right)_P = \frac{n_2^2 \frac{\mu_{r1}}{\mu_{r2}} \cos\theta - n_1\sqrt{n_2^2 - n_1^2 \sin^2\theta}}{n_2^2 \frac{\mu_{r1}}{\mu_{r2}} \cos\theta + n_1\sqrt{n_2^2 - n_1^2 \sin^2\theta}}. \tag{2.10}$$

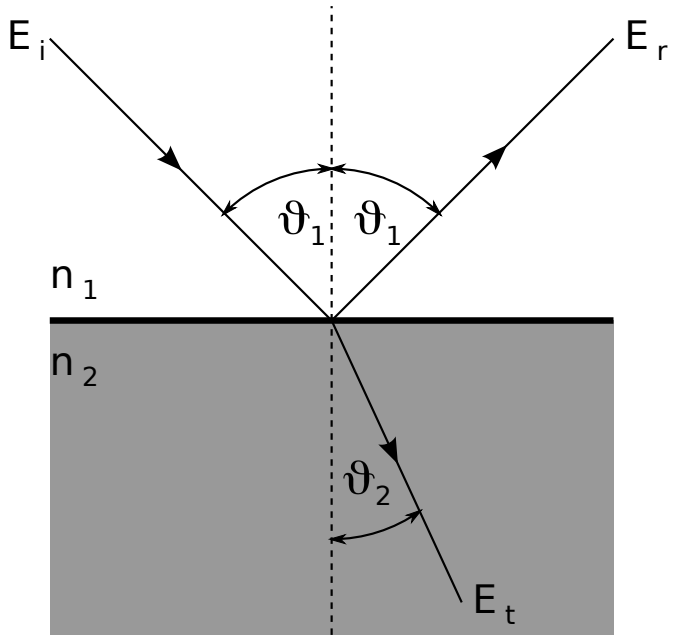

Figure 2.3: Reflection on a plane surface with $n_1 < n_2$.

These equations are dependent on the polarisation of the incident light, either perpendicular (S) or parallel (P), the incident energy E_{0i}, the incidence angle θ, the refraction values n_1,n_2 of the two media and the relative magnetic permeability μ_{r1},μ_{r2} of the media. In the case of non-magnetic materials with $\mu_r \approx 1$, the reflectivity (2.8) and (2.10) can be written as

$$R_S = \left| \frac{n_1 \cos\theta - n_2 \sqrt{1 - (\frac{n_1}{n_2} \sin\theta)^2}}{n_1 \cos\theta + n_2 \sqrt{1 - (\frac{n_1}{n_2} \sin\theta)^2}} \right|^2 , \tag{2.11}$$

$$R_P = \left| \frac{n_1 \sqrt{1 - (\frac{n_1}{n_2} \sin\theta)^2} - n_2 \cos\theta}{n_1 \sqrt{1 - (\frac{n_1}{n_2} \sin\theta)^2} + n_2 \cos\theta} \right|^2 . \tag{2.12}$$

Fig. 2.4 shows the behaviour of these equations for changing incidence angles. The transmittivity of the surface can be calculated from the reflectivity by $T = 1 - R$. However, reflection is not the only process that reduces the transmitted energy, another important process is the absorption of light in a medium. This absorption can be strongly dependent on the wavelength of the incident light as discussed in Sec. 2.1.2. The intensity of a light beam after passing through a material with the thickness L and the absorption coefficient α can be calculated following the *Lambert-Beer* law

$$I(\lambda, L) = I_0 e^{-\alpha(\lambda) L}, \tag{2.13}$$

where I_0 is the initial intensity and λ the wavelength of the beam. However, Snellius' law and the Fresnel equations are designed in the model of ray optics, to describe the behaviour of

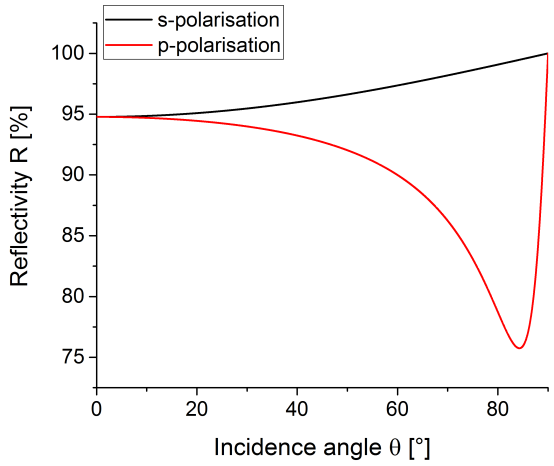

Figure 2.4: Reflectivity profile of (2.11) and (2.12) for different incidence angles with $n_1 = 1$ and $n_2 = 1.38 + 10i$.

electromagnetic waves in materials, the concept of wave optics has to be used. This concept builds on the four Maxwell equations

$$\nabla \times \mathbf{E} = -\mu_0 \mu \frac{\partial \mathbf{H}}{\partial t}, \tag{2.14}$$

$$\nabla \times \mathbf{H} = \epsilon_0 \epsilon \frac{\partial \mathbf{E}}{\partial t} + \sigma \mathbf{E}, \tag{2.15}$$

$$\nabla \cdot (\epsilon \mathbf{E}) = 0, \tag{2.16}$$

$$\nabla \cdot (\mu \mathbf{H}) = 0, \tag{2.17}$$

with the vector fields $\mathbf{E}$ and $\mathbf{H}$ for the electric field and the magnetic field respectively, the electric conductivity σ, the electric permittivity ϵ and the magnetic permeability μ. From these basic equations the wave functions for electromagnetic waves can be derived as

$$\begin{aligned} 0 = \Delta \mathbf{E} + \nabla [\mathbf{E} \cdot \nabla (\ln \epsilon)] - \frac{\epsilon \mu}{c^2} \frac{\partial^2 \mathbf{E}}{\partial t^2} \\ - \mu_0 \mu \sigma \frac{\partial \mathbf{E}}{\partial t} + [\nabla (\ln \mu)] \times (\nabla \times \mathbf{E}) \end{aligned} \tag{2.18}$$

for the electric field and

$$\begin{aligned} 0 = \Delta \mathbf{H} + \nabla [\mathbf{H} \cdot \nabla (\ln \mu)] - \frac{\epsilon \mu}{c^2} \frac{\partial^2 \mathbf{H}}{\partial t^2} \\ - \mu_0 \mu \sigma \frac{\partial \mathbf{H}}{\partial t} + [\nabla (\ln \epsilon)] \times (\nabla \times \mathbf{H}) \\ + [\nabla \sigma - \sigma \nabla (\ln \epsilon)] \times \mathbf{E} \end{aligned} \tag{2.19}$$

for the magnetic field. Assuming a time-harmonic, wave with angular frequency ω,

$$\mathbf{E}(\mathbf{r}, t) = \hat{\mathbf{E}}(\mathbf{r}) e^{-i\omega t} \tag{2.20}$$

$$\mathbf{H}(\mathbf{r}, t) = \hat{\mathbf{H}}(\mathbf{r}) e^{-i\omega t} \tag{2.21}$$

as solutions to the wave functions leads to an expression of (2.18) and (2.19).

$$\begin{aligned} 0 =& \Delta\hat{\mathbf{E}} + \nabla\left[\hat{\mathbf{E}}\cdot\nabla(\ln\epsilon)\right] + \omega^2\frac{\epsilon\mu}{c^2}\hat{\mathbf{E}} + i\omega\mu_0\mu\sigma\hat{\mathbf{E}} \\ &+ [\nabla(\ln\mu)]\times\left(\nabla\times\hat{\mathbf{E}}\right), \end{aligned} \tag{2.22}$$

$$\begin{aligned} 0 =& \Delta\hat{\mathbf{H}} + \nabla\left[\hat{\mathbf{H}}\cdot\nabla(\ln\mu)\right] + \omega^2\frac{\epsilon\mu}{c^2}\hat{\mathbf{H}} + i\omega\mu_0\mu\sigma\hat{\mathbf{H}} \\ &+ [\nabla(\ln\epsilon)]\times\left(\nabla\times\hat{\mathbf{H}}\right) + [\nabla\sigma - \sigma\nabla(\ln\epsilon)]\times\hat{\mathbf{E}}. \end{aligned} \tag{2.23}$$

These expressions describe the time-independent behaviour of the electromagnetic field in linear and isotropic materials and are called the *Helmholtz* equations.

2.2.2 Laser Ablation

Ablation occurs when the absorbed energy of the laser beam exceeds the binding energy of the atoms in the irradiated solid.

$$\Delta H^a[J/\text{atom}] = \frac{\Delta H[J/g]}{N_s} \approx \frac{\Delta H_v[J/g]}{N_s}, \tag{2.24}$$

where ΔH_v is the enthalpy of evaporation at the boiling temperature of the solid and N_s is the atom number density. This energy, though, is only an upper estimate, as collective effects, hydrodynamic instabilities and stress relaxation in the material may reduce the required energy per atom significantly. The excess energy of the ejected material will go into its kinetic energy and eventually into internal energy, e.g. ionisation. Collisions within the first few mean free paths after ejection from the surface (*Knudsen layer*) will lead to thermalisation of the evaporated material. As a simple model the expansion of the vapor can be described by an adiabatic gas expansion [7], where the temperature in the plume decreases with distance from the target surface, while the expansion velocity of the plume increases up to a maximum value.
The material ejected from the surface will, in accordance with Newton's third law, create a recoil pressure on the surface, which will transfer a certain amount of pressure into the solid, causing shock waves in the solid, while ejecting portions of the molten surface layer for ultra short pulses and evaporating the material for longer pulse durations.
In a one dimensional ablation model the laser beam propagates in z-direction, while the material surface is located along the $z = 0$ plane and the influence of plasma in the plume is neglected. Considering a laser pulse of the length τ_l and a uniform intensity of the laser beam on the material surface, the laser-induced surface temperature can be estimated by the one dimensional heat equation in a reference frame moving with $v(t)$ and being attached to the material surface

$$\rho c_p\left(\frac{\partial T}{\partial t} - v\frac{\partial T}{\partial z}\right) = \frac{\partial}{\partial z}\left(\kappa_s\frac{\partial T}{\partial z}\right) - \frac{\partial I}{\partial z}, \tag{2.25}$$

with the mass density ρ, the specific heat capacity c_p, the average temperature T at which the ablation occurs, the intensity of the laser beam I and the heat conductivity κ_s depending on the phase of the material. When ignoring heat transport in the liquid by convection, the boundary condition

$$-\kappa_s\frac{\partial T}{\partial z}\,|_{z=0} = S_s = -J_i\Delta H_v^a(T_s), \tag{2.26}$$

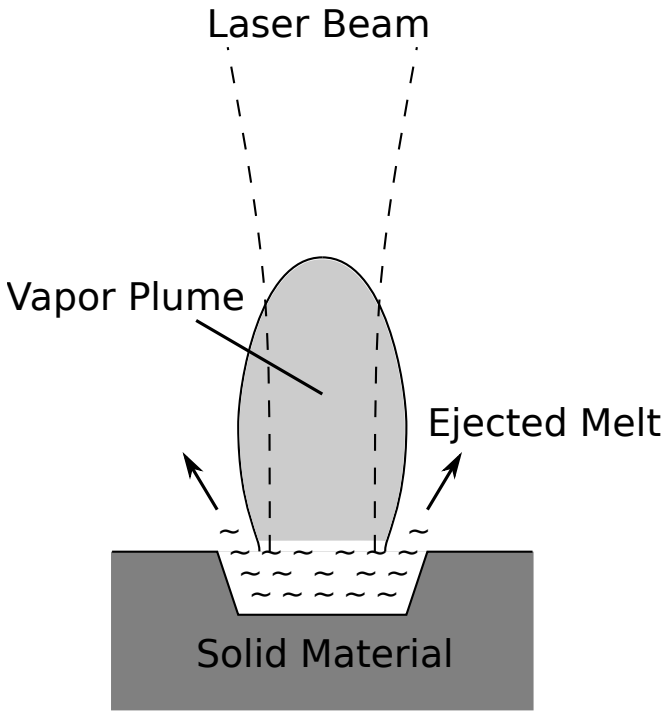

Figure 2.5: Topology of the ablation process (redrawn from [6])

with the material flux J_i, the total energy flux on the surface S_s and the surface temperature T_s, leads to

$$\frac{\partial \Delta H_s}{\partial t} = v\frac{\partial \Delta H_s}{\partial z} + \frac{\partial}{\partial z}\left(\kappa_s \frac{\partial T}{\partial z}\right) - \frac{\partial I}{\partial z}, \tag{2.27}$$

where H_s is the total enthalpy of the material. This leads to a temporal behaviour of the surface temperature and ablation front velocity (v) that is depicted in fig 2.6.
[6] shows that the minimum absorbed fluence of the laser light, required to initiate an ablation process can be calculated as

$$\Phi_a^{min} = \frac{\Delta H_s(T_{st})}{\alpha}, \tag{2.28}$$

where T_{st} is the stationary temperature reached during ablation and α is the optical absorption coefficient of the irradiated material depending on the wavelength of the laser light.

2.3 Two Temperature Model

Metals almost exclusively absorb light by electron transitions in their conduction band. The time scale in which the energy is distributed among the electrons is typically below one picosecond. Thermalisation between the electron subsystem and the ion lattice, however, is a lot slower, typically in the range of up to 100 picoseconds, depending on the electron-phonon coupling of the material. A detailed description of the processes can be found in [6].
For laser pulses with pulse lengths below this coupling time, the rapid energy deposition in the electron system leads to a hot electron gas with temperature T_e and an ion lattice, that is yet

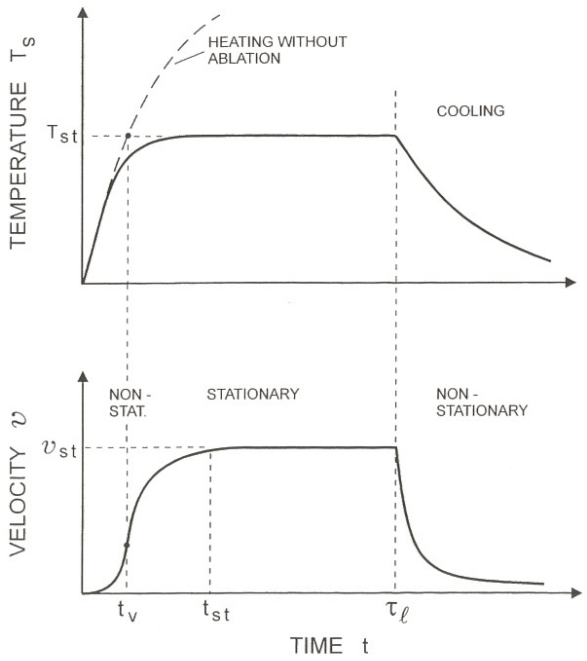

Figure 2.6: Temporal evolution of surface temperature T_s and ablation front velocity v. Expected temperature rise without evaporation is depicted as dashed curve. τ_l is the pulse length of the laser, t_v and t_{st} are the times required to reach a stationary value for the temperature and the velocity respectively, showing that a stationary temperature is achieved much sooner than a stationary velocity [6]

to be affected by the laser energy and retains its temperature T_i. This non-equilibrium between the two connected subsystems leads to a relaxation that can be described by

$$C_e \frac{\partial T_e}{\partial t} = \nabla(\kappa_e \nabla T_e) - \Gamma_{\text{e-ph}}(T_e - T_i) + Q(x_\alpha, t), \tag{2.29}$$

$$C_i \frac{\partial T_i}{\partial t} = \nabla(\kappa_i \nabla T_i) + \Gamma_{\text{e-ph}}(T_e - T_i). \tag{2.30}$$

Here C_i and C_e are the heat capacities of the lattice and the electron subsystems respectively, while κ_e and κ_i describe the heat conductivity of each system and $\Gamma_{\text{e-ph}}$ is the coupling coefficient between the electron and the phonon system. The source term Q describes the heating process by the incident laser beam and can be approximated by

$$Q(z,t) = \alpha A I(t) \exp(-\alpha z), \tag{2.31}$$

for a one dimensional case.
The simulations of this thesis used pulse durations in the femto- and picosecond range, which exhibit an interesting behaviour.

2.3.1 Femtosecond Pulse

In the regime of femtosecond laser pulses, the pulse duration is short compared to the time scale in which the electron gas is cooled by energy transport into the lattice. While calculating

the system in this time frame ($t \ll \tau_e = C_e/\Gamma_{\text{e-ph}}$), the electron-phonon coupling can hence be ignored, so that (2.29) can be simplified to

$$\frac{1}{2}C_0\frac{\partial T_e^2}{\partial t} = \alpha I_a \exp(-\alpha z), \tag{2.32}$$

with $C_0 = C_e/T_e$ for electron temperatures far below the Fermi temperature. From this, the electron temperature is exclusively dominated by the source term and can be calculated as

$$T_e(t) = \left[T_0^2 + \frac{2\alpha\phi_a(t)}{C_0}\exp(-\alpha z)\right]^{1/2}, \tag{2.33}$$

where ϕ_a is the absorbed fluence of the laser in the electron gas. After the full pulse length τ_l, the electron temperature can be approximated by ignoring the initial temperature T_0 since it will be dominated by the source term, leading to

$$T_e(\tau_l) \approx \left(\frac{2\alpha\phi_a}{C_0}\right)\exp\left(-\frac{\alpha z}{2}\right). \tag{2.34}$$

The evolution of the system for times larger than the pulse length can be calculated by using (2.29) and (2.30) leading to an expression for the lattice temperature

$$T_i \approx \frac{\alpha\phi_a}{C_i}\exp(-\alpha z). \tag{2.35}$$

2.3.2 Picosecond Pulse

In the regime of picosecond pulses, the pulse length is much larger than the time scale of heat conduction by electrons. Therefore, the electron temperature becomes quasi stationary $\partial T_e/\partial t \approx 0$. When taking into account the heat conduction by the electrons, (2.30) leads to

$$T_i(0,t) \approx \frac{\phi_a(t)}{C_i(l_e + l_\alpha)}\exp\left(-\frac{1}{\tau_{ph}}\right), \tag{2.36}$$

with $\tau_{ph} = C_i/\Gamma_{\text{e-ph}}$, l_e being the diffusion length of the heated electrons (see [6]) and l_α being the absorption depth of the laser beam. In the case of surface absorption ($l_\alpha \ll l_e$) and $\tau_l \ll \tau_{ph}$ the maximum lattice temperature at the end of the pulse can be approximated as

$$T_i(0,\tau_l) \approx \frac{\phi_\alpha}{C_i l_e}. \tag{2.37}$$

It is to be noted that the general problem of (2.29) and (2.30) can only be solved numerically.

3 Software Details

The simulation tools used during this thesis are a molecular dynamics code developed at the former Institute for Theoretical and Applied Physics at the University of Stuttgart, called IMD and a hydrodynamic code developed at the Joint Institute for High Temperatures at the Russian Academy of Sciences. Though both simulation tools were used for the same purposes during this thesis, their structures and capabilities differ vastly.

3.1 Molecular Dynamics and IMD

IMD was developed by the former *Institut für Theoretische und Angewandte Physik* at the university of Stuttgart. It was initially designed to provide an open source tool for simulating quasi-crystals using the molecular dynamic formalism but has been expanded ever since to provide functionality beyond its initial purpose. It provides a simulation model for classical molecular dynamics in two or three dimensions and is designed to make use of multi-core systems such as super computers or modern desktop computers to distribute its calculation load. The informations presented in this part can be found at [8] and [9].

3.1.1 Molecular Dynamics - Basics

Molecular dynamics in general is used to simulate point like particles, that are assigned spatial coordinates and vectorial velocities, whose interactions are calculated via interaction potentials. All relevant properties of the particle interactions have to be included in these potentials to ensure the simulation to be as close to reality as possible. The potentials used in this thesis are tailored towards the interactions in simple metals like aluminium and gold and are based on the *Embedded Atom Model*. These potentials take into account the interactions between an atom and its closest neighbours, while introducing a cut-off for longer ranges, thus creating a multi-body problem that can only be solved numerically. For any given atom inside such a system this EAM-potential can be described as

$$V_i = \frac{1}{2} \sum_{ij, i \neq j} \phi(r_{ij}) + F\left(\sum_j \rho(r_{ij}) \right), \tag{3.1}$$

where ϕ contains the interaction between the cores of atoms i and j and F describes the interaction of the electron hull of atom i with all its neighbours while influenced by the local electron density $\rho(r_{ij})$. In the case of aluminium the behaviour of these three functions is shown in Fig. 3.1.
From these potentials the forces acting on each atom can be calculated using

$$\mathbf{F} = -\nabla V(\mathbf{r}). \tag{3.2}$$

In molecular dynamics these forces are used to solve Newton's equations of motion by using so called *integrators*, which solve these equations of motion for every time step. IMD, which is

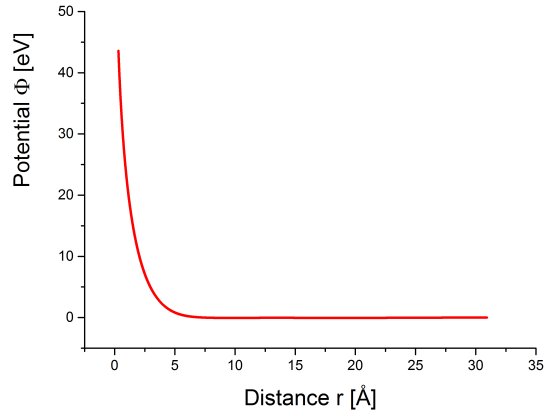

(a) Core-Core potential ϕ

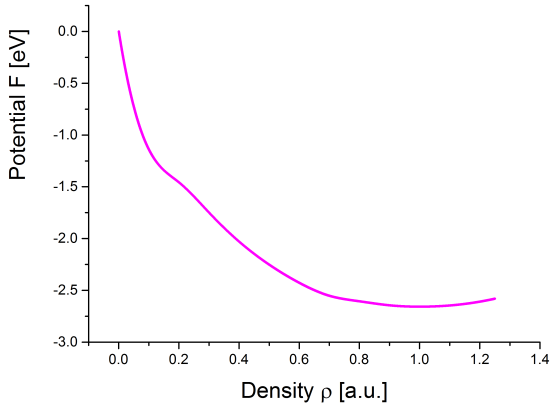

(b) Electron hull potential F

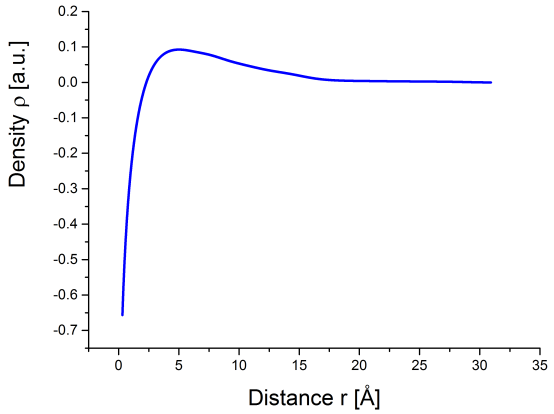

(c) Local electron density ρ

Figure 3.1: Behaviour of the core to core and electron hull potentials as well as the electron density comprising the EAM-potential for Aluminium as presented in [10]

the molecular dynamics code used during this thesis, utilises a *leapfrog integrator* scheme for its calculation:

$$\mathbf{r}(t+\Delta t) = \mathbf{r}(t) + \frac{\Delta t}{m}\mathbf{p}(t+\frac{1}{2}\Delta t), \tag{3.3}$$

$$\mathbf{p}(t+\frac{1}{2}\Delta t) = \mathbf{p}(t-\frac{1}{2}\Delta t) + \mathbf{F}\cdot\Delta t. \tag{3.4}$$

3.1.2 Two Temperature Model in IMD

The laser-matter interaction in IMD can be calculated using the Two Temperature Model described in 2.3 thus using equations (2.29) and (2.30) to calculate the energy transport in the system. These equations, however, describe the energy transport only in continuum mechanics while IMD is calculating interactions in a model of discrete point-like elements such as atoms. To avoid this issue the electron system is calculated in a *finite difference scheme* (FD) emulating a continuum to solve (2.29) while the ionic system is calculated in the molecular dynamics environment, thus leading to a hybrid model of the form

$$C_e(T_e)\frac{\partial T_e}{\partial t} = \nabla[\kappa_e \nabla T_e] - \Gamma_{e-ph}(T_e - T) + Q(\mathbf{r}, t), \tag{3.5}$$

$$m_i \frac{\partial^2 \mathbf{r_i}}{\partial t^2} = \mathbf{F_i} + \xi m_i {\mathbf{v_i}}^T, \tag{3.6}$$

where (3.5) calculates the electron temperature in the FD system, while (3.6) describes the forces acting on the atoms in the MD system, caused by the energy exchange between the electron and the ion system, where m_i and $\mathbf{r_i}$ are the mass and position of the i-th atom in the molecular dynamics ensemble. The force $\mathbf{F_i}$ is derived from the inter-atomic potentials (see (3.1)) and a thermal velocity ${\mathbf{v_i}}^T = \mathbf{v_i} - \mathbf{v}_{CM}$ is introduced which relates the velocity of each atom $\mathbf{v_i}$ to the center of mass velocity $\mathbf{v}_{CM}$ of the atoms inside the FD cell. The coupling between the FD and MD system is done by a modified coupling parameter

$$\xi = \frac{\frac{1}{n}\sum_{k=1}^{n} \Gamma_{e-ph} V_N (T_{e,k} - T)}{\sum_j m_j (v_j^T)^2}. \tag{3.7}$$

The FD system is evaluated more often than the MD system, with n being the number of FD time steps done during one MD time step. k is used to sum over all FD time steps while j is used to sum over all atoms inside the FD cell. To prevent the MD system to draw to much or to few energy out of the FD system a condition for the number of FD steps compared to one MD step has to be met.

$$n \geq \frac{2\Delta t \kappa_e}{\chi_{FD} \min[C_e]}, \tag{3.8}$$

Δt being the time of one MD time step, χ_{FD} the minimum thickness of one FD cell and $\min[C_e]$ the minimum electron heat capacity during the simulation.

3.1.3 Transport Properties

The key parameters describing the energy transport from the electron subsystem into the ion subsystem as shown in (3.5) and (3.6) are the heat capacity of the electron system C_e, the thermal conductivity of the electron system κ_e and the coupling parameter between the two subsystems $\Gamma_{\text{e-ph}}$. These parameters are assumed to be temperature dependent, their implementation in IMD however is

- $C_e(T) \rightarrow \gamma \cdot T$,
- $\kappa_e(T_e) \rightarrow \kappa_e = \text{constant}$,
- $\Gamma_{\text{e-ph}}(T_e, T_i) \rightarrow \Gamma_{\text{e-ph}} = \text{constant}$.

The results from this implementation have shown to be in good agreement with experiments for laser pulses in the femtosecond range and low fluences, however, diverge from experimental data for pulse lengths of picoseconds and longer.

3.1.4 Optical Properties

The temporal course of the laser fluence in IMD follows a gaussian function, where the peak intensity *laser_sigma_e* and the half duration of the laser pulse *laser_sigma_t* are defined in the parameter file. This fluence is the one just below the surface, thus all optical effects outside of the material and at the surface are neglected, e.g. reflection. Absorption in the material is treated by the Lambert-Beer law (2.13) with a constant optical absorption coefficient α.

3.2 Hydrodynamics and Polly-2T

Polly-2T was developed at the *Joint Institute for High Temperatures* at the Russian Academy of Sciences in Moscow. It was designed as a dedicated tool for simulating laser-matter interaction in a hydrodynamic formalism utilising a wide-range numerical model which was developed on the basis of the two temperature model including heat transport, ionisation, plasma expansion, electron-ion collisions and two-temperature equations of state for the irradiated material. The source for this chapter was [11].

3.2.1 Governing Equations

Polly-2T uses a set of conservation equations written in a one dimensional Lagrangian form and using the two temperature model described in Sec. 2.3.

$$\frac{\partial V}{\partial t} - \frac{\partial u}{\partial m} = 0, \tag{3.9}$$

$$\frac{\partial u}{\partial t} + \frac{\partial (P_i + P_e)}{\partial m} = 0, \tag{3.10}$$

$$\frac{\partial e_e}{\partial t} + P_e \frac{\partial u}{\partial m} = -\gamma_{ei}(T_e - T_i)V + Q_L V + \frac{\partial}{\partial m}\left(\kappa \frac{\partial T_e}{\partial z}\right), \tag{3.11}$$

$$\frac{\partial e_i}{\partial t} + P_i \frac{\partial u}{\partial m} = \gamma_{ei}(T_e - T_i)V, \tag{3.12}$$

with V being the material specific volume, m the mass coordinate, t the time, z the spatial coordinate, u the velocity, P_e and P_i the electron and ion pressure respectively and e_e and e_i the specific energies of the electrons and ions. The parameters from the TTM include γ_{ei} as the coupling coefficient between the electron and ion system, the electron thermal conductivity κ, the temperatures of the electron (T_e) and ion (T_i) system and the source term Q_L describing the energy deposition by absorption of the laser light in the conduction band of the irradiated metal.

3.2.2 Two Temperature Model in Polly-2T

In Polly-2T the TTM has been implemented by the afore mentioned governing equations in the form of (3.11) and (3.12), though heat capacity for the electron and ion subsystems have been moved into the EOS. The thermal conductivity of the ions is neglected due to the rather low contribution compared to the electron thermal conduction.

3.2.3 Transport Properties

To calculate the energy transported from the electron system into the ion system Polly-2T utilises a wide-range model to describe the key parameters governing this transport over a wide range of temperatures. In this wide-range model it is assumed that the transition of the material

from the metal phase into the plasma phase occurs in the vicinity of the Fermi temperature T_F. Under this assumption the thermal conductivity can be written as an interpolation between the behaviour in the metal phase and the behaviour in the plasma phase:

$$\kappa = \kappa_{pl} + (\kappa_{met} - \kappa_{pl}) e^{-A_4^t T_e / T_F}, \tag{3.13}$$

with $A_4^t = 1.2$, the conductivity in the plasma phase κ_{pl}, the conductivity in the metal phase κ_{met} and the electron temperature T_e. In the metal phase κ_{met} can be calculated according to the Drude-formalism as

$$\kappa_{met} = \frac{\pi^2 k_B^2 n_e}{3 m_e \nu_{\mathrm{eff,t}}} T_e, \tag{3.14}$$

with the electron concentration n_e, the electron mass m_e, the electron temperature T_e and the effective collision frequency $\nu_{\mathrm{eff,t}}$. This frequency is defined as

$$\nu_{\mathrm{eff,t}} = \min[\nu_{met}, \nu_{max}], \tag{3.15}$$

$$\nu_{met} = \frac{A_1^t k_B T_i}{\hbar} + \frac{A_2^t k_B T_e^2}{T_F \hbar}, \tag{3.16}$$

$$\nu_{max,p} = \frac{A_3^t}{r_0} \sqrt{\frac{v_F^2 + k_B T_e}{m_e}}, \tag{3.17}$$

where $A_1^t = 2.95$, $A_2^t = 0.5$ and $A_3^t = 0.16$, T_i is the ion temperature, r_0 is the interatomic distance and v_F is the Fermi speed of electrons.
In the plasma phase κ_{pl} can be calculated as

$$\kappa_{pl} = \frac{16\sqrt{2} k_B (k_B T_e)^{5/2}}{\pi^{3/2} Z e^4 \sqrt{m_e} \Lambda}, \tag{3.18}$$

where Z is the mean charge of the ions, e is the elementary charge and Λ is the Coulomb logarithm.
The coupling parameter γ_{ei} then follows as

$$\gamma_{ei} = \frac{3 k_B m_e}{m_i} n_e \nu_{\mathrm{eff,g}}, \tag{3.19}$$

with the effective frequency, defined as $\nu_{\mathrm{eff,g}} = \min[\nu_{\mathrm{met,g}}, \nu_{\mathrm{max,g}}, \nu_{pl}]$. The maximum frequency and the frequency in the metal phase can be calculated similar to (3.16) and (3.17), with empirical parameters $A_1^g = 50.0$, $A_2^g = 20$ and $A_3^g = 0.25$. Plasma frequency ν_{pl} can be described by

$$\nu_{pl} = \frac{4}{3} \sqrt{2\pi} \frac{Z n_e e^4 \Lambda}{\sqrt{m_e} (k_B T_e)^{3/2}}. \tag{3.20}$$

3.2.4 Optical Properties

Polly-2T uses the same wide-range model used for the thermal conductivity (3.13) to calculate the electric permittivity of the target material ϵ as an interpolation between ϵ_{met} in the metal phase and ϵ_{pl} in the plasma phase

$$\epsilon = \epsilon_{pl} + (\epsilon_{met} - \epsilon_{pl}) e^{-A_4^p T_e / T_F}, \tag{3.21}$$

where the permittivity in the metal phase is composed of the band-to-band contribution ϵ_{bb} which read from a table and an intraband term

$$\epsilon_{met}(\omega_L, \rho, T_i, T_e) = \epsilon_{bb} + 1 - \frac{n_e}{n_{cr}(1 + i\,\nu_{\text{eff,p}}/\omega_L)}, \tag{3.22}$$

where ω_L is the frequency of the laser, ρ is the density of the material and n_{cr} is the critical concentration of electrons. The effective frequency of collision $\nu_{\text{eff,p}}$ can be calculated according to (3.15) - (3.17). The parameter $A_1^p = 4.41$ has been adjusted to match experimental values at room temperature, while $A_2^p = 0.8$, $A_3^p = 0.7$ and $A_4^p = 0.2$ have chosen to describe experiments on self reflectivity.
In the plasma phase, for temperatures far above the Fermi one, the permittivity can be calculated as

$$\epsilon_{pl}(\omega_L, \rho, T_e) = 1 - \frac{n_e}{n_{cr}} \left[K_1(\xi) - i \left(\frac{\nu_{pl}}{\omega_L} \right) K_2(\xi) \right], \tag{3.23}$$

where $K_1(\xi)$ and $K_2(\xi)$ are empirical values with $\xi = 3\sqrt{\pi}\frac{\nu_{pl}}{4\omega_L}$.
Calculations of laser absorption and reflectivity are done using wave optics, especially the *Helmholtz* equations for linear materials, (2.22) and (2.23). It is assumed that $n = \sqrt{\epsilon_r}$ for non-magnetic materials and a depth dependent $\epsilon(z)$ is introduced leading to a z-dependent formulation for the electric and the magnetic field in the case of S-polarisation and P-polarisation respectively:

$$\frac{\partial^2 E}{\partial z^2} + k_0^2[\epsilon(z) - \sin^2\theta]E = 0, \tag{3.24}$$

$$\frac{\partial^2 B}{\partial z^2} + k_0^2[\epsilon(z) - \sin^2\theta]B - \frac{\ln \epsilon(z)}{\partial z}\frac{\partial B}{\partial z} = 0, \tag{3.25}$$

where E is the single component electric field envelope $E(z,t) \equiv E_y(z,t)$, B is the single component magnetic field envelope $B(z,t) \equiv B_y(z,t)$ and $\mathbf{k_0} = (\omega_L/c)\{\sin\theta, 0, \cos\theta\}$. With these equations for the electromagnetic field components the source term in (3.11), describing the absorption of the laser field, can be written as

$$Q_L(z) = \frac{\omega_L}{8\pi} \text{Im}[\epsilon(z)]\,|\mathbf{E}(z)|^2, \tag{3.26}$$

with $|\mathbf{E}|^2 = \left|\mathbf{E_y}\right|^2$ for S-polarised beams and $|\mathbf{E}|^2 = |\mathbf{E_x}|^2 + |\mathbf{E_z}|^2$ for P-polarised beams, by using the correlation between the electric and the magnetic field components

$$E_z = -B_y \frac{\sin\theta}{\epsilon}, \tag{3.27}$$

$$E_x = -\frac{i}{\epsilon k_0}\frac{\partial B_y}{\partial z}. \tag{3.28}$$

The electric field is calculated from the fluence via the intensity, where the temporal profile of the fluence is read from the parameter file.

3.3 Summary - Comparison of IMD and Polly-2T

Though both programs can be used to simulate the interaction of laser beams with matter, IMD and Polly-2T utilise completely different frameworks. The essential differences are in the physical description used in the codes, IMD uses a classical molecular dynamics approach, which deals with point like particles and the classical forces acting on them via interaction potentials, while Polly-2T uses hydrodynamics, that use the description of continuum mechanics, where the interactions are calculated by the equations of state under the constraints of conservation laws. This also leads to different implementations of the Two Temperature Model, as the original formulation (2.29) (2.30) is done with macroscopic parameters and thus fits the hydrodynamic approach of Polly-2T while in IMD certain modifications have to be included (3.6) to account for the microscopic formulation of molecular dynamics. Polly-2T also uses a wide-range model to calculate the transport parameters of the TTM (3.13) and (3.19) while in IMD it is assumed that these parameters are constant. On the optics side IMD features the *Lambert-Beer* law to describe the absorption of laser energy in the material, while Polly-2T uses the *Helmholtz* equations to describe reflection and absorption of the laser field and also introduces a wide-range model to calculate the electric permittivity (3.21). The temporal profile of the fluence in IMD is that of a gaussian, while Polly-2T offers the possibility to use different pulse shapes as they can be defined by the user in the parameter file.

Table 3.1: Comparison between IMD and Polly-2T

Feature	**IMD**	**Polly-2T**
Physical description in	Interaction potentials	EOS
Formalism	discrete elements	continuum mechanics
TTM	macroscopic/microscopic hybrid	macroscopic
electron thermal conductivity κ_e	constant	wide-range model
coupling coefficient γ_{ei}	constant	wide-range model
optics	absorption	reflection + absorption
laser absorption	Lambert-Beer law	Helmholtz equations
electric permittivity ϵ	n.a.	wide-range model
temporal fluence profile	gaussian	user defined

The differences between the two codes become obvious when comparing TTM and absorption parameters at room temperature for IMD and Polly-2T, Tab. 3.2.

Table 3.2: Comparison of TTM and absorption parameters in IMD and Polly-2T at room temperature 300 K, $\lambda = 1064$ nm . [4], [11]

Parameter	**IMD**	**Polly-2T**
absorption coefficient $\alpha \left[\frac{1}{m}\right]$	$1 \cdot 10^8$	$1.26662 \cdot 10^8$
electric permittivity ϵ	n.a.	$-111.876 + 37.1745\ i$
electron thermal conductivity $\kappa_e \left[\frac{J}{smK}\right]$	235	359.75
coupling parameter $\gamma_{ei} \left[\frac{J}{sm^3K}\right]$	$5.69 \cdot 10^{17}$	$3.8 \cdot 10^{17}$
electron heat capacity $c_e(T_e) \left[\frac{J}{m^3K}\right]$	$135 \cdot T_e$	in EOS

4 Approach for an Upgrade of IMD

The goal for upgrading IMD is to enhance the validity of its simulation of laser matter interaction beyond the range of femtosecond laser pulses. The current version of IMD, however, lacks certain essential features to accomplish that, as shown in Tab. 3.1. Polly-2T, on the other hand, supports these features, but is only capable of a one dimensional representation of the interactions. Since IMD can be used for one-dimensional as well as three-dimensional calculations, Polly-2T will serve as a basis for validating the results gained by the upgraded version of IMD in one-dimensional mode. To gain a valid comparison between these two rather different codes, Polly-2T has to be downgraded to deactivate some of its higher features, while IMD is upgraded stepwise to include the required features. As IMD progresses to include more of the above mentioned features, the downgrades in Polly-2T will be deactivated again to match the new capabilities of IMD.

Table 4.1: Simplified feature overview prior to the upgrade

Feature	IMD	Polly-2T
Surface optics (Fresnel equations)	×	✓
iterative calculation of ϵ	×	✓
iterative calculation of γ_{ei} and κ_e	×	✓
ionisation states	×	✓

Three essential milestones and one optional have been defined for the upgrade of IMD.

4.1 Cold Reflectivity

Cold reflectivity describes the fixed reflectivity of the material at room temperature. This upgrade introduces the incidence angle of the laser beam θ as a new feature in IMD as well as the polarisation of the laser beam and the reflectivity of the material surface R. This is done by using the Fresnel equations for both polarisation types and complex refraction indices (eqn.(2.11),(2.12)). At this step the refraction index does not change and is set during the start of the simulation. To validate the results of this upgrade, the iterative calculation of the material permittivity ϵ and the TTM parameters κ_e and γ_{ei} in Polly-2T is deactivated (see Tab. 4.2).

Table 4.2: Feature overview for "cold" reflectivity

Feature	IMD	Polly-2T
Surface optics (Fresnel equations)	✓	✓
iterative calculation of ϵ	×	×
iterative calculation of γ_{ei} and κ_e	×	×
ionisation states	×	✓

4.2 Dynamically Changing Reflectivity

This upgrade builds on the cold reflectivity and uses a tabulated evolution of the refraction index to simulate the dynamic changes of the refraction index and, therefore, the reflectivity during runtime. To validate this upgrade, the table, listing the evolution, is generated using Polly-2T while its iterative calculation of κ_e and γ_{ei} is deactivated and the results are compared (see Tab. 4.3).

Table 4.3: Feature overview for dynamically changing reflectivity, with o denoting a partially implemented feature (see above)

Feature	IMD	Polly-2T
Surface optics (Fresnel equations)	✓	✓
iterative calculation of ϵ	o	✓
iterative calculation of γ_{ei} and κ_e	×	×
ionisation states	×	✓

4.3 Temperature-dependent Energy Absorption

As seen in equations (3.21),(3.22) and (3.23), the permittivity and thus the refraction index in the Two Temperature Model is dependent on the electron and ion temperature, the laser frequency and the local density. In this upgrade step these parameters are calculated for each FD-cell during each simulation step and used to derive the refraction index and calculate the amount of laser-energy absorbed in each cell. At this point only the calculations of the electron heat conductivity and the TTM coupling constant are deactivated for Polly-2T as shown in Tab. 4.4.

Table 4.4: Feature overview for temperature dependent reflectivity

Feature	IMD	Polly-2T
Surface optics (Fresnel equations)	✓	✓
iterative calculation of ϵ	✓	✓
iterative calculation of γ_{ei} and κ_e	×	×
ionisation states	×	✓

4.4 Optional Goal

If there is enough time after these upgrade steps, the same methods used in the third upgrade step can be used to enable IMD to iteratively calculate the κ_e and γ_{ei} according to (3.13) and (3.19). A comparison between IMD and the original version of Polly-2T should now only result

in differences caused by the loss of kinetic energy due to ionisation, which would still be missing in IMD (see Tab. 4.5), since the current interaction potentials don't support ionisation states in their calculations.

Table 4.5: Feature overview for optional goal

Feature	**IMD**	**Polly-2T**
Surface optics (Fresnel equations)	✓	✓
iterative calculation of ϵ	✓	✓
iterative calculation of γ_{ei} and κ_e	✓	✓
ionisation states	×	✓

5 IMD Bugs

In [4] it was discussed, that IMD simulations yield considerable deviations to Polly-2T for higher fluences and longer pulse durations. This was attributed to the interaction potentials in IMD being developed for states adjacent to the normal state and not considering the plasma state, as well as the missing implementation of the ionization process in IMD and therefore no reduction in the systems thermal or kinetic energy due to changes in the ionization states. These higher kinetic energies in IMD lead to particles reaching velocities beyond the capabilities of the potentials, resulting in errors ending the simulations.
During this thesis the absorbed energy of the simulations performed for [4] was analysed by calculating the change in total energy of the system

$$E_{\mathrm{abs}} = E_{\mathrm{pot}} + E_{\mathrm{th}} + E_{\mathrm{el}} - E_{\mathrm{init}} \tag{5.1}$$

where E_{pot} is the potential energy of the system, E_{th} the thermal energy of the lattice structure, E_{el} the energy stored in the electronic part of the two temperature model and E_{init} the initial energy of the system at the start of the simulation. The absorbed energy of beams with a pulse duration of $\tau = 500$ fs, with its contributions to the total energy is illustrated in Fig. 5.1, though the behaviour for pulse lengths of 50 fs and 5 ps is similar. Fig. 5.1 shows that although the absorbed energy is specified in the parameter file by the values indicated with the *input*-line, the energy gain of the simulation is higher and the deviations seem to be increasing with higher fluences. Since the thermal energy is coupled to the energy in the electron system through the two temperature model, the energy in the electron system should decrease by the same amount the thermal energy and the potential energy are increased, thus resulting in a constant absorbed energy after the pulse. As we can see this holds for Fig. 5.1(a) and 5.1(b) with the exception of a small spike around the pulse maximum, while Fig. 5.1(c) still shows an increase in absorbed energy 30 ps after the pulse and and Figures 5.1(d) and 5.1(e) show a completely erratic behaviour in their electronic energy. Since these simulations were done using the original IMD code, it is to be assumed, that this behaviour for higher fluences is fundamental issue of the two temperature model in IMD and will be present in all upgrade steps. Therefore, the results discussed in the following chapter have to be analysed while keeping this bug of IMD's two temperature model in mind.
Another know bug of IMD occurs while simulating larger fluences on multiple CPUs. The heating process will accelerate some atoms to such velocities that at the beginning of the next time step the atom has skipped one CPU in its path. This leads to an error in IMD and the simulation crashes. The occurrence of this bug might be amplified by the bug in the two temperature model.

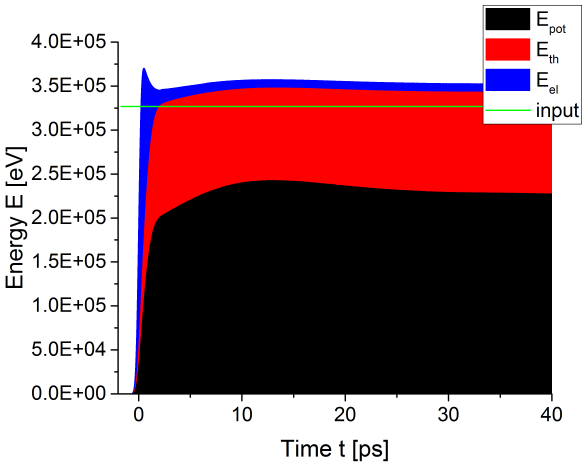

(a) Absorbed fluence $\Phi_{\text{abs}} = 0.18 \frac{\text{J}}{\text{cm}^2}$

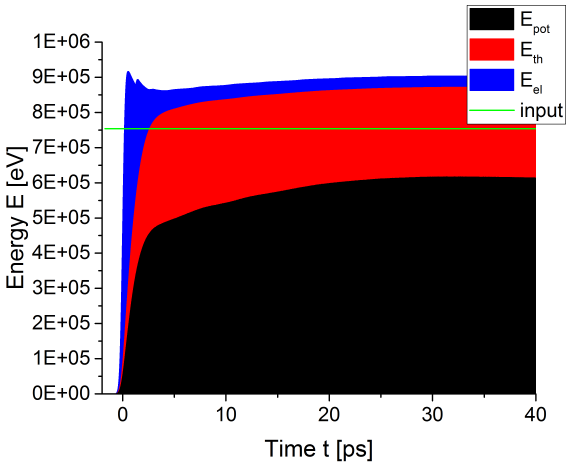

(b) Absorbed fluence $\Phi_{\text{abs}} = 0.37 \frac{\text{J}}{\text{cm}^2}$

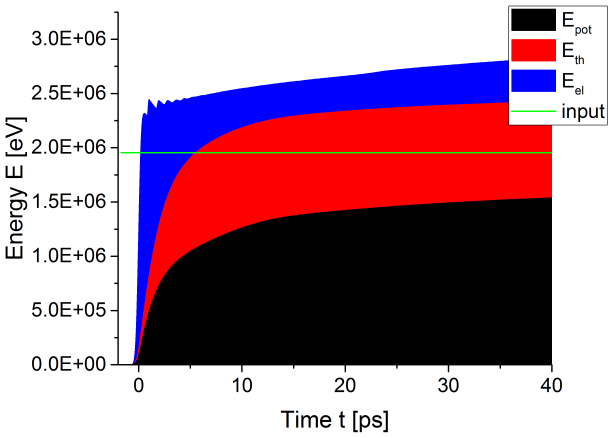

(c) Absorbed fluence $\Phi_{\text{abs}} = 0.74 \frac{\text{J}}{\text{cm}^2}$

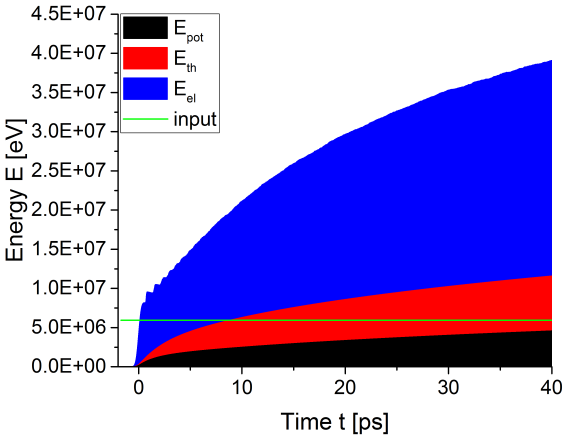

(d) Absorbed fluence $\Phi_{\text{abs}} = 1.49 \frac{\text{J}}{\text{cm}^2}$

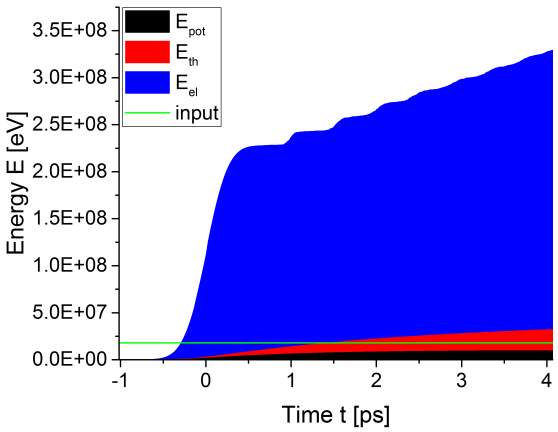

(e) Absorbed fluence $\Phi_{\text{abs}} = 2.97 \frac{\text{J}}{\text{cm}^2}$

Figure 5.1: Energy distribution for simulations in [4], with $\tau = 500$ fs and irradiated surface area of $A = 400$ nm^2. *input* gained from Polly-2T simulation.

6 Results

Following the outlined approach in Ch. 4, the upgrade was carried out in steps. Each step implemented further modifications to the IMD code to include the Fresnel equations and the wide-range model for the electric permittivity, the electron thermal conductivity and the electron-phonon coupling. This is followed by simulations in IMD and Polly-2T with comparable parameter sets to verify the results obtained with the upgrade by using Polly-2T as the benchmark.

6.1 Cold Reflectivity

During the first upgrade step (see Sec.4.1), minor changes were applied to the function reading the input parameters and a method was implemented to calculate the absorbed energy from the laser fluence by considering losses due to reflection. To simplify the work flow of setting up a simulations in IMD and Polly-2T a utility tool for generating the required parameter files was created using *Wolfram Mathematica*.

6.1.1 IMD Upgrades

In the initial version of IMD the absorbed fluence *sigma_e* was directly specified in the parameter file, requiring the user to calculate the reflectivity and thus the effectively absorbed fluence before the simulation could be started. To begin the upgrade, a variety of new parameters have been defined:

- laser_fresnel = on or off, to switch between the original code and the upgraded version,
- laser_polarisation = polarisation of the laser beam, either s or p,
- laser_phi = output fluence of the laser, in J/cm^2,
- laser_nreal = real part of the complex refraction index of the irradiated material,
- laser_nimag = imaginary part of the complex refraction index of the irradiated material and
- laser_theta = incidence angle of the laser beam in degree.

With these parameters the reflectivity of the material surface is calculated using the Fresnel equations for non-magnetic materials (2.11) and (2.12). The influence of incidence angle and polarisation on the reflectivity are shown in Fig. 2.4. The incidence angle of the beam also influences the effective fluence at the surface, called *surface fluence* Φ_{surf}, by an increase of the spot size at larger angles. The result is a decrease in the surface fluence, which can be calculated using $\Phi_{\text{surf}} = \Phi_{\text{laser}} \cdot \cos\theta$. This so-called *spot size correction* was implemented in IMD during the first test runs of the upgrade. After the first test runs it was decided to move this feature into the parameter file generator and change the upgraded IMD code to directly use the surface fluence as input parameter.

The absorbed fluence is then calculated from the surface fluence by $\Phi_{abs} = (1-R)\cdot\Phi_{surf}$. For the implementation of the Fresnel equations and accompanying parameters see App. **??**. To reduce complications during parsing the energy into the FD cells, the original framework was kept intact. Also all parameters were converted into IMD units (see Tab. 10.1) to keep consistency of the unit system throughout the code.
To be able to start simulations with different parameter sets, the parameters from the list above were included as new parameters in the parameter file. This was achieved by using the existing framework of IMD to read the new parameters from the file and parse them to the appropriate functions.

6.1.2 Polly-2T Downgrades

To have a benchmark for the results generated with the upgraded version of IMD, a number of features in Polly-2T had to be deactivated. The first feature to be shut down, was the temperature dependent calculation of the permittivity ϵ. This was achieved by implementing a new parameter in the Polly-2T parameter file, similar to the IMD parameter laser_fresnel, used to switch between the unmodified code and the upgrade. The switch in Polly-2T was done by overloading the function calculating the permittivity, to return a constant ϵ if it was called with additional parameters including the complex refraction index and calculating ϵ from this n.
To further increase the comparability of the modified IMD code with Polly-2T, the heat conductivity κ and TTM-coupling parameter γ_{ei} were also set as constants by defining them in the parameter file.
A modification to the parameter read-out function was also required to ensure the new parameters were read correctly.

6.1.3 Parameter File Generator

Since the number of options and parameters required to start an IMD simulation can be rather extensive a solution to procedurally generate parameter files was devised. The Param-file-generator was written in *Mathematica* and provides a graphical interface with procedural generated windows. The user has to specify which options he wishes to use in the simulation, the file-generator will only ask for the general IMD parameters and the parameters required for the chosen options. To further increase user friendliness pre-sets can be defined, loaded and altered. The script facilitates quality management by printing the user's name and date of generation in the header of the parameter file as well as the version of the generator script used. The script is capable of generating a bash-script required for analysing the IMD output data and can also be set to generate a parameter file for Polly-2T that runs a hydrodynamic simulation with starting parameters comparable to the IMD simulation.

6.1.4 Simulation

The goal of the *Cold Reflectivity* upgrade was to implement the Fresnel equations in IMD. The simulation parameters were chosen to test this new feature. All IMD simulations were run, using the same surface fluence, while the only varied parameters were the incidence angle and the polarisation. Since Polly-2T uses the laser fluence as input parameter, it had to be ensured, that

the surface fluence would be the same as in IMD. Therefore higher laser fluences were required to compensate the drop in surface fluence for greater angles (see Tab. 6.1). To further increase the comparability the downgrade steps for fixed permittivity, electron thermal conductivity and electron phonon coupling were activated with

- permittivity $\epsilon = 110 + 38i$
- electron thermal conductivity $\kappa_e = 235\ \frac{\mathrm{W}}{\mathrm{K\,m}}$
- electron-phonon coupling parameter $\gamma_{ei} = 0.569\ 10^{-12} \frac{\mathrm{kW}}{\mathrm{kK\ cm^3}}$

Table 6.1: Simulation set ups for the *Cold Reflectivity* upgrade. All simulations used a surface fluence $\Phi_{\mathrm{surf}} = 0.74$ J/cm^2, a Gaussian pulse profile with a pulse length $\tau = 50$ fs and a complex refraction index of $1.38 + 10i$. Varied parameters were the incidence angle θ and the polarisation. The table also includes the absorbed fluences in IMD and Polly-2T.

Simulation	θ [°]	**Pol.**	Φ_{laser} [J/cm^2]	$\Phi_{\mathrm{abs,IMD}}$ [J/cm^2]	$\Phi_{\mathrm{abs,Polly\text{-}2T}}$ [J/cm^2]
Sim_th0	0	s	0.74	0.050	0.039
Sim_th20p	20	p	0.79	0.053	0.041
Sim_th20s	20	s	0.79	0.047	0.036
Sim_th40p	40	p	0.97	0.066	0.050
Sim_th40s	40	s	0.97	0.037	0.030
Sim_th60p	60	p	1.48	0.100	0.074
Sim_th60s	60	s	1.48	0.024	0.020
Sim_th80p	80	p	4.26	0.228	0.157
Sim_th80s	80	s	4.26	0.008	0.007

Fig. 6.1 shows the behaviour of the relative absorbed fluence as expected from the Fresnel equations. If the implementation of the reflectivity according to the Fresnel equations has been successful, the absorbed energies of both simulation tools should follow the behaviour described by equations (2.11) and (2.12).

6.1.5 Data Analysis

To analyse the simulation data generated with IMD and Polly-2T, post processing is necessary as both simulation tools generate vast amounts of data. Since the focus is on the absorbed fluence, the parameter needed to be compared for our simulations is the change in the total energy of the simulated system. Due to the use of periodic boundary conditions in IMD, we can assume our ensemble to be a closed system, thus any energy induced by the laser beam should stay within the system. The first test runs used the IMD option *pdecay*, which serves as a sink for kinetic energy of the particles deep in the target, to reduce the amplitude of pressure waves and their reflection at the back surface of the target. This is needed for longer simulations to

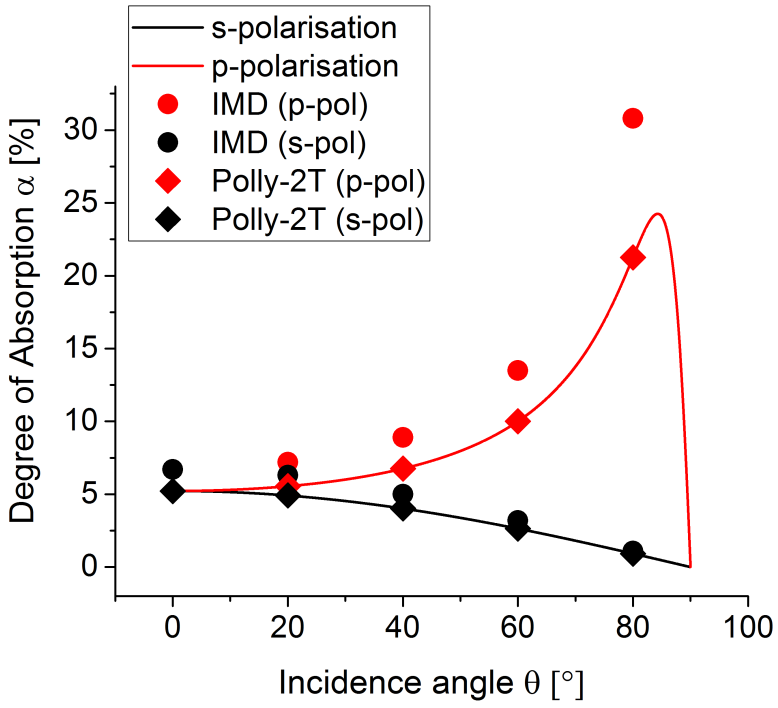

Figure 6.1: Comparison of the degree of absorption predicted by the Fresnel equations and calculated with IMD and Polly-2T.

emulate infinite target depth, since the simulations in this thesis have short simulation times during which the pressure waves do not reach the back surface of the 650 nm deep target, the option was deactivated to better analyse the energy distribution of the system.
IMD generates *.eng* files which list for every simulation step how the energy is distributed among the potential energy, the thermal energy of the atoms, which is calculated from their kinetic energy and the thermal energy of the electron system in the two temperature model. By subtracting the starting energy of the system from the total energy, one can plot the evolution of the induced energy corresponding to the absorbed beam energy using equation (5.1). The corresponding absorbed fluence Φ_{abs} can be calculated using

$$\Phi_{\text{abs}} = E_{\text{abs}}/A_{\text{target}} \tag{6.1}$$

where A_{target} is the surface area of the irradiated target. In Polly-2T the absorbed fluence can be read from one of the output files (*name*_pulse.dat). By dividing the absorbed fluences of Tab. 6.1 by the incident surface fluence of $\Phi_{\text{surf}} = 0.74$ J/cm^2, the data can be compared to the behaviour of the Fresnel equations for different incidence angles and polarisation. Fig. 6.1 shows that the downgraded version of Polly-2T with its deactivated wide-range model for permittivity, electron thermal conductivity and electron-phonon coupling follows the behaviour of the Fresnel equations very accurately. The absorbed energy gained with the upgraded version of IMD shows some deviations from the theoretical values. For s-polarisation the values are slightly elevated compared to the theory and Polly-2T, where deviations for p-polarisation seem to be even more elevated. However, this is in agreement with the findings in Ch.5, where we discovered, that IMD will exhibit a bigger error in the absorbed energy with increasing fluence. Since the Fresnel equations lead to increased absorbed fluences for p-polarisation and incidence angles up to $\approx 85°$, the deviations from Polly-2T and the theoretical model can be attributed

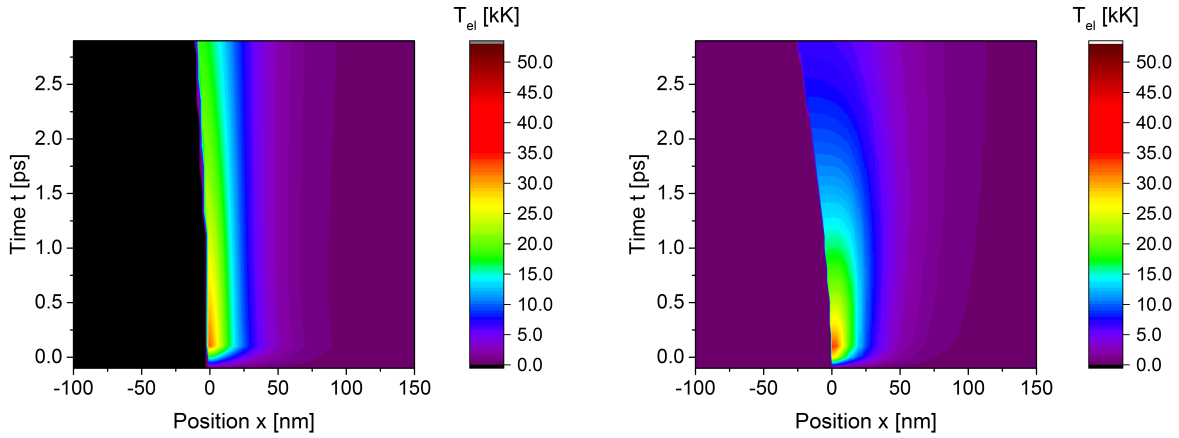

(a) Electron temperature IMD

(b) Electron temperature Polly-2T

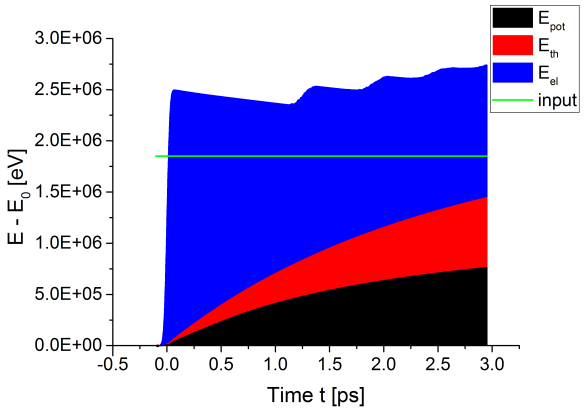

(c) Energy gain of the IMD simulation

Figure 6.2: Comparison between the evolution of the electron temperature T_{el} in IMD and Polly-2T and the energy gain of the IMD simulation with its contributions, at an incidence angle of 60° and p-polarisation.

to the implementation of the two temperature model in IMD and its problems with handling higher fluences.

By comparing the evolution of the electron temperatures of IMD and Polly-2T, we can see that even though Polly-2T uses fixed electron thermal conductivity and electron-phonon coupling with values equal to those in IMD, it takes the IMD simulation far longer to dissipate thermal energy from the electron system than in Polly-2T (see Fig. 6.2(a) and Fig. 6.2(b)). From Fig. 6.2(c) we see, that the electron energy of the two temperature model is still increasing at the end of the simulation. Since the electron temperature is directly linked to the electron energy of the two temperature model, we can assume, that the increase of electron energy discussed in Ch.5 and seen in Fig. 6.2(c) is the cause of the observed severe discrepancy between the behaviour of the electron temperature for IMD and Polly-2T, as both simulations use the same thermal conductivity and electron-phonon coupling coefficients.

6.1.6 Conclusion

The data from Fig. 6.1 indicate that the implementation of fixed angular and polarisation dependent reflectivity in IMD was successful. IMD simulations now reproduce the general behaviour of the Fresnel equations and Polly-2T in its downgraded state, though the amount of energy gained in IMD is always larger than predicted by Polly-2T and the Fresnel equations. However, this discrepancy can be attributed to the problems IMD encounters at higher fluences as discussed in Ch.5. We see that the fluence $\Phi_{\text{surf}} = 0.74$ J/cm^2, which was used for the test of the cold reflectivity upgrade, is an intermediate case where the electron energy already starts to increase even after the pulse, yet is not doing so in the severity as observed for higher fluences. Thus, we see a qualitative agreement between IMD and Polly-2T, yet discrepancies in the quantitative behaviour of the two simulation tools.
Further differences between the evolution of the electron temperature in IMD and Polly-2T should arise from the different implementation of the thermal capacity, however, the temperature behaviour in IMD seems to be largely dominated by the bug in the two temperature model.

6.2 Dynamic Reflectivity

For the second upgrade step the time dependence of the reflectivity for a given parameter set was extracted from a Polly-2T simulation with fixed κ_e and γ_{ei}. This could be done by loading the output file of Polly-2T containing the evolution of optical parameters into *Origin* and then exporting the columns containing the time stamp and the reflectivity. For future applications a script utilizing the Linux Bash was devised that can read a given Polly-2T output file and generate the required table for the use in IMD. IMD was then upgraded to read these reflectivity values and modulate the laser fluence similar to the previous upgrade step. This step served as a test to see how a variable reflectivity would affect the IMD simulations and if further upgrade steps would be feasible.

6.2.1 IMD Upgrade

To use the tables containing the reflectivity a new parameter had to be implemented in the parameter file, specifying the name of the file holding the reflectivity table. The next step was to write a function that would read the table and save its content into a data structure which can be accessed during the simulation. This function is called *get_TSV_data* and can recognize the unit of the time column if it is given in the header. It then converts the time data into femtoseconds and saves time and associated reflectivity in an array structure. The next function required for this upgrade is an interpolation function that utilizes a linear interpolation scheme to calculate the reflectivity for any given time using the data in the array. At this point it became apparent that the implementation of the dynamic reflectivity could not be done at the same point the previous upgrade had been implemented. To increase clarity of the code a new implementation was done in a part of the code that is called every time step and not just at the beginning of the simulation as in the previous upgrade step. A switch function was then used to allow for switching between the different upgrades and the unaltered IMD calculation from the parameter file (see Fig. 6.3). This upgrade relies heavily on the use of Polly-2T in advance, as the given evolution of reflectivity holds true only for a specific combination of laser fluence, pulse length, incidence angle and polarisation.

6.2.2 Simulation

Simulations for this feature were done by first running a Polly-2T simulation with the desired surface fluence Φ_{surf}, pulse length τ, incidence angle θ and polarisation. The file containing the reflectivity data (*name*_pulse_0.dat) is then processed by the shell-script (Reflectivity.sh) to extract only the reflectivity data and the time stamp for each reflectivity value. This new file is named like the simulation it is taken from and has the extension *.rfl*. This rfl-file is then specified in the IMD parameter file. Since the upgraded IMD code will calculate the energy absorbed in the material by using the reflectivity obtained from Polly-2T it is assumed to be sufficient to have one working simulation, to prove that the reading and application of the reflectivity data is working as intended. The parameters chosen for this simulation were a laser fluence of $\Phi_{\text{laser}} = 0.74$ J/cm^2, a pulse length of $\tau = 500$ fs, an incidence angle of $\theta = 0°$ and s-polarisation.

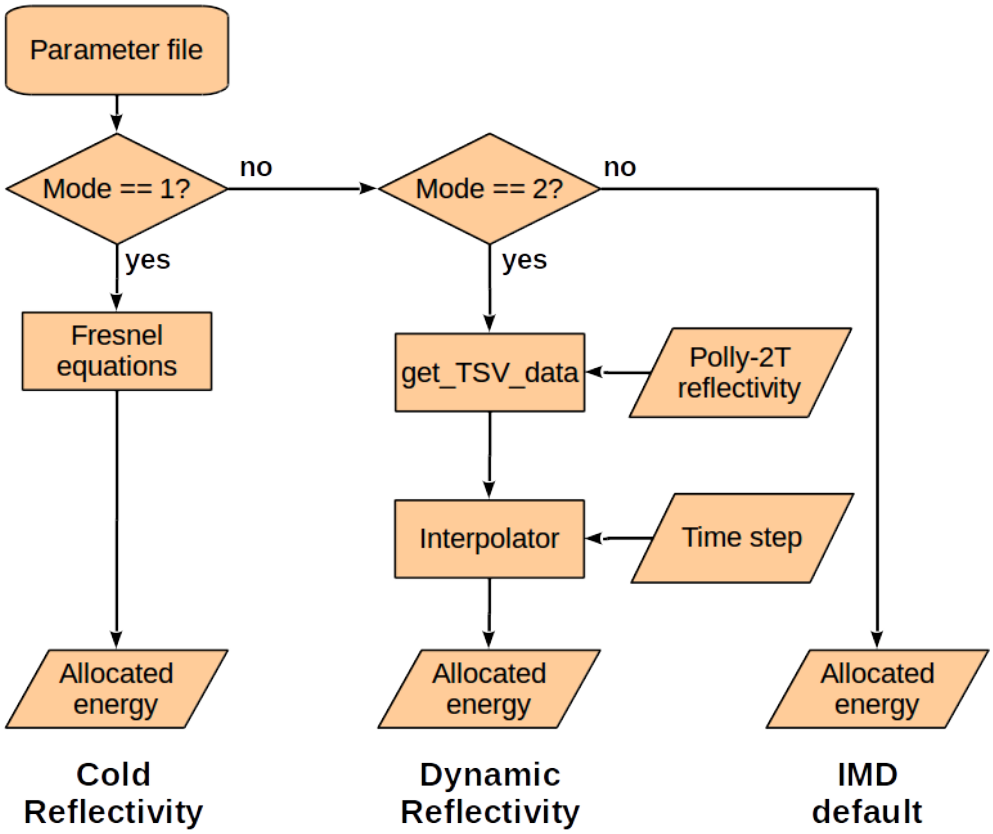

Figure 6.3: Structure of the upgraded laser energy allocation during the dynamic reflectivity upgrade step.

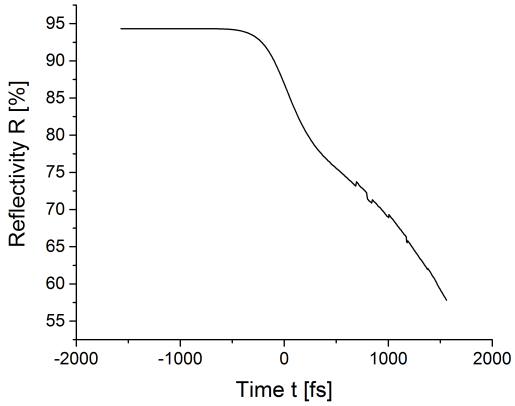

(a) Evolution of aluminium reflectivity calculated with Polly-2T.

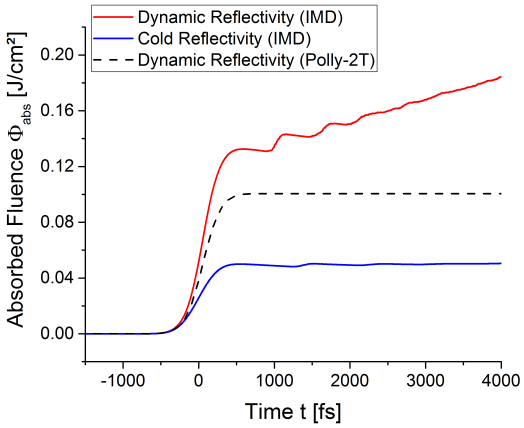

(b) Comparison of the energy profiles for IMD with dynamic reflectivity and cold reflectivity.

Figure 6.4: Influence of dynamic reflectivity on an IMD simulation with a surface fluence of $\Phi_{surf} = 0.74$ J/cm^2 and pulse length of $\tau = 500$ fs.

6.2.3 Data Analysis

Fig. 6.4(a) shows the evolution of the reflectivity Polly-2T generates with the given parameter set. As expected the reflectivity drops due to material heating during the pulse. At the pulse maximum (0 in Fig. 6.4(a)) the reflectivity has dropped from 94.3% to 86.9%. This leads to higher energy absorption during the pulse compared to a constant reflectivity at room temperature. Fig. 6.4(b) shows this behaviour for an IMD simulation with the cold reflectivity upgrade and IMD with the dynamic reflectivity upgrade.
To check if the absorbed energy in the downgraded version of Polly-2T is influenced by other factors than the reflectivity, the evolution of the time dependent reflectivity values obtained from the simulation is multiplied with the time dependent function of the beam intensity. Since these theoretical predictions are virtually identical to the Polly-2T results, we can assume the the evolution of the absorbed energy in Polly-2T is dominated by the behaviour of the reflectivity.
In Fig. 6.4(b) we can see that during the pulse ($\tau = 500$ fs) the absorbed fluence in IMD with dynamic reflectivity is closer to the absorbed fluence of Polly-2T than the cold reflectivity version. The rise in absorbed fluence after the pulse in IMD with dynamic reflectivity can be attributed to the influence of the TTM bug encountered at higher fluences.

6.2.4 Conclusion

The data generated with this upgrade shows, that the implementation of a time-dependent reflectivity in IMD produces higher energy gains than the same simulation with cold reflectivity. The upgraded IMD code follows the behaviour established by the downgraded Polly-2T code and the theoretical prediction with some deviations due to the bug in the two temperature model. This leads to the conclusion, that the implementation of a time dependent reflectivity in IMD has been successful and the implementation of the wide-range model for calculating the

absorption coefficient and reflectivity is a viable next step. The data also shows, that even for pulses with relative short pulse lengths of a few hundred femtoseconds, the allocated energy is influenced by the changes in the reflectivity. Due to the coupling time between the electron and ion system the discrepancy between cold reflectivity and dynamic reflectivity is assumed to increase with the pulse length. A more quantitative analysis of the IMD data is still prevented by the bug in the two temperature model, as the electron energy again shows an unphysical increase after the pulse.

6.3 Temperature-Dependent Energy Absorption

The third upgrade step required extensive changes to the IMD code, concerning the way energy absorption is handled as well as the structure of the cells used in the finite difference part of the two temperature calculation. For this a new method for allocating the beam energy to each cell was devised, the methods for calculating the electric permittivity according to the wide-range model, equations (3.21) - (3.23) as well as several supporting functions were implemented and the constructor for the FD-elements had to be adjusted to accept the real and imaginary part of the permittivity as additional values of a FD-cell.

6.3.1 Upgraded Energy Absorption Scheme

In the original version of IMD energy absorption was handled by calculating the depth of every FD-cell inside the bulk material and using the Lambert-Beer law to calculate the amount of energy reaching the cell at its current depth.
This, however, assumed a constant absorption coefficient along the depth of the material. Considering the inhomogeneous spatial distribution of temperature in the target and the resulting spatial dependence of the permittivity, the absorption coefficient can not be assumed constant if the wide-range model for the permittivity is to be implemented.
To derive a new scheme for the energy allocation with varying absorption values, we start from the Lambert-Beer law, since a constant absorption coefficient should still reproduce the old results. We then split the continuous depth d into n parts of equal length Δd.

$$e^{-\mu\, d} = e^{-\mu\, n\, \Delta d} \tag{6.2}$$

$$= e^{-\mu\, (\Delta d + \Delta d + \ldots)} \tag{6.3}$$

$$= e^{-\mu\, \Delta d} \cdot e^{-\mu\, \Delta d} \cdot e^{-\mu\, \Delta d} \cdot \ldots \tag{6.4}$$

From (6.4) we can see that if we assume n to be the number of cells the beam has to pass through and Δd to be the length of one cell, we can assign one Lambert-Beer like term to every cell beginning with the first cell. Following this, each cell can be assigned a different absorption coefficient and by iteratively calculating the remaining beam energy we can get the energy at any given cell along the absorption path (see Fig. 6.5).

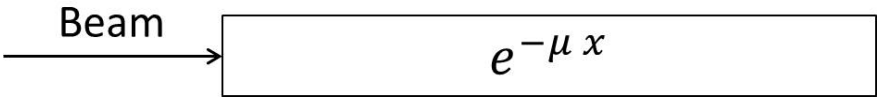

(a) Original IMD scheme

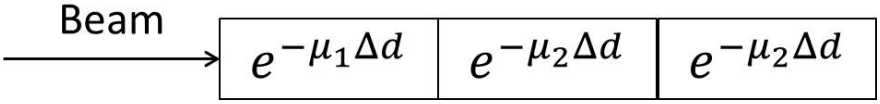

(b) Upgraded scheme

Figure 6.5: Schematic of the beam absorption in the original IMD and the upgraded version.

To implement this iterative approach into the three dimensional grid structure of the FD-cells,

a scheme was devised that assumes the absorption path to be oriented only in the X direction. For each Y-Z-coordinate the scheme initializes the beam energy at the surface cell of the bulk material and calculates the reflection using Fresnel's formulas. Incidence angle and polarisation are read from the parameter file, while the complex refraction index is calculated from the permittivity of the cells and the laser wavelength. This excludes ablated material from the energy allocation process since the beam will only be initialized at the surface of the bulk. A cell is considered a bulk cell if it possesses one active neighbour cell in each X-direction. The reason for this is that otherwise reflection had to be calculated at every boundary, which would have been far more time intensive and was not feasible in the time of this thesis. The method then calculates the remaining energy after the cell, by using the scheme from (6.4) with the absorption coefficient

$$\mu = \frac{4\pi \cdot \Im\left[\sqrt{\epsilon}\right]}{\lambda} \tag{6.5}$$

which is obtained from the cell's permittivity and the length of the cell in X direction. It will then iterate to the next cell in X direction, use the reduced beam energy as incident energy and again use Lambert-Beer's law to calculate the absorption inside the cell. This is repeated until the end of the X space is reached and the method jumps to the next Y-Z-coordinate (see Fig. 6.6).

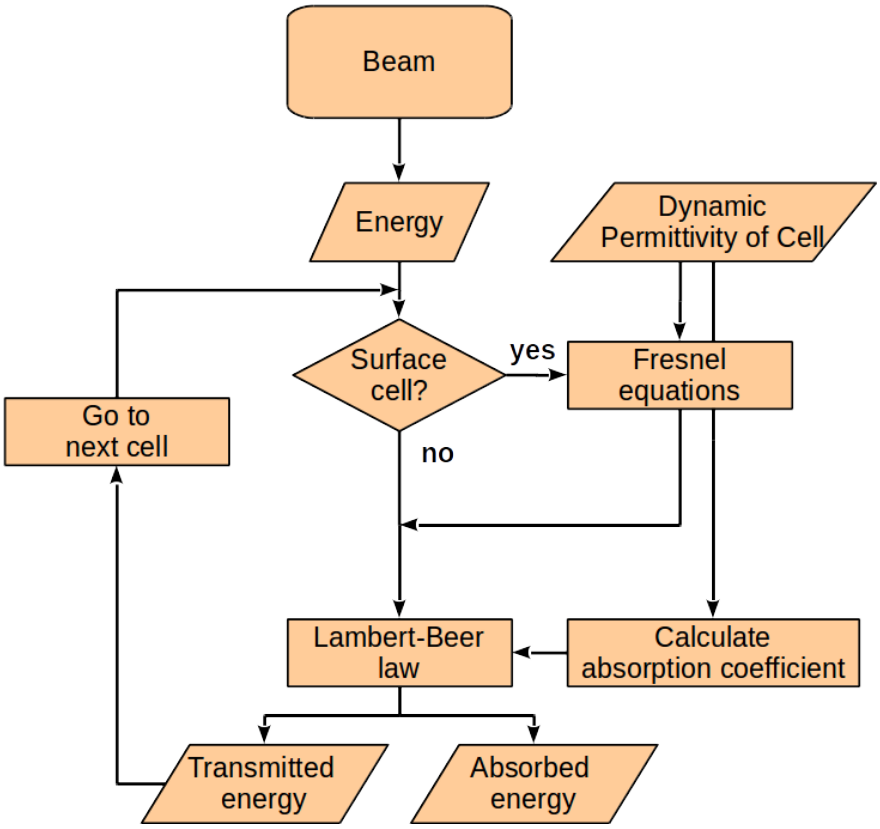

Figure 6.6: Schematic of the iterative energy allocation method

6.3.2 Implementation of the Wide-Range Model for ϵ

The implementation of the wide-range model for the electric permittivity in IMD is based on the implementation in Polly-2T and the formulas presented in [11]. This implementation uses additional data from two tables containing material specific coefficients. To read these tables a general function was developed, that can import a specified number of columns from a file into a given array.
The next step was to implement the supporting functions for the calculation of ϵ, these functions calculate certain properties required during the actual wide-range calculation. They include functions to calculate the

- Fermi energy E_F,
- Fermi temperature T_F,
- interatomic distance $r0$,
- plasma frequency ν_{pl},
- coulomb logarithm Λ,
- critical electron density n_{cr},
- mass density in the FD-cell ρ and
- the mean charge in the cell Z.

These are followed by the collision frequencies (3.17), (3.16) and (3.20). For all of these functions it is important to keep track of the unit system they work in, as Polly-2T uses CGS most of the time, while IMD uses its own unique system (see 10.1). To achieve this, every function for the wide-range model is written using SI units. At the beginning of every method, the arguments are translated from IMD-units into SI and are translated back into IMD-units at the return part of the method, this keeps the formulas in the code easily accessible, yet does not conflict with IMD's native unit system. The actual calculation of the wide-range model is done by using formulas (3.21), (3.22) and (3.23).
To store the calculated epsilon values for each cell the constructor of the FD-cells had to be upgraded to allow these structures to hold two additional parameters, the real and imaginary part of the complex permittivity.
IMD separates its FD-cells into active and inactive ones. Where a cell counts as active if a certain number of atoms in the cell is exceeded. The calculation of the two temperature model occurs only in active cells, therefore the implementation of the permittivity could only be done for active cells as well, otherwise the electron temperature of the cell would not be accessible. The allocation of the permittivity to each active FD-cell occurs in the upgraded update method of the two temperature module, which updates all values stored in the cell structure after each time step.

6.3.3 Further Changes to IMD

The parameter file had to be extended again to accept the new parameters laser wavelength and the name of the material data table. Changes were also done to the output files generated by the

two temperature module, to have the permittivity appended to the output of every FD-cell. The previous upgrades were kept as well, to be able to use the desired upgrade mode. The upgrade can be chosen by setting a flag in the parameter file called *laser_reflectivity_mode*. This extends the schematic in Fig. 6.3 to the one in Fig. 6.7.

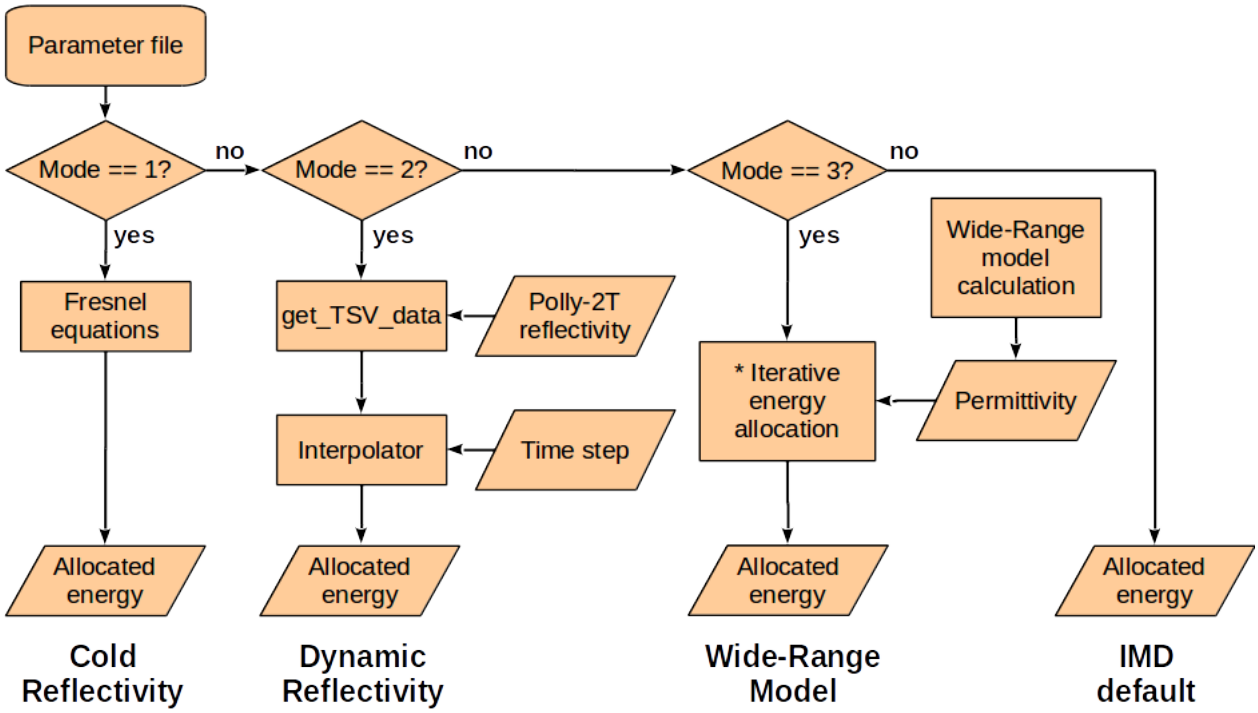

Figure 6.7: Schematic of the different upgrades inside the IMD code and their respective methods of calculating the allocated energy.
* The iterative energy allocation of the third mode can be seen in Fig. 6.6.

6.3.4 Known Issues

The implementation of the new energy allocation scheme has a draw-back, as it is impossible to use with multiple processors in its current state. In multi-processor mode IMD will distribute certain areas of the simulation space to different CPUs. The way simulation space is distributed can be specified in the parameter file. Since splitting in Y and Z direction caused the simulation to crash during runtime only splitting along the X-axis is considered viable. However, that means that every CPU along the X-axis will run the energy allocation method separately, since no communication method for multiple CPUs could be implemented to this point. Running the energy allocation separately, causes every CPU that contains active cells to initialize the beam when the first active cell is encountered. The results of this missing communication can be seen in Fig. 6.8, as each red spot depicts the initialization and allocation of beam energy in a different CPU. The workaround for this issue was to run simulations only on a single CPU, thus increasing the time it took a simulation to complete considerably.
A proper solution for this problem would be to implement a communication between the CPUs using the mpi protocol IMD uses for its parallelization. This communication should verify that the beam is only initialized once per X-lane and the remaining beam energy at the end of the CPU is parsed to the following ones.

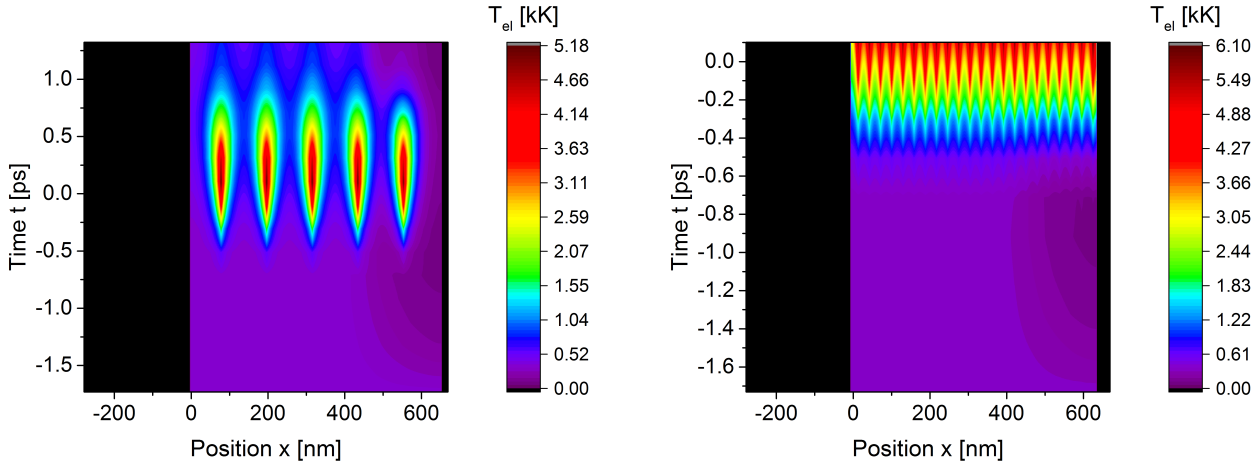

(a) Energy allocation with parallelization on 8 CPUs

(b) Energy allocation with parallelization on 32 CPUs

Figure 6.8: First tests with the new energy allocation scheme. Simulations were done with the same parameter sets but parallelized on a different number of CPUs.

6.3.5 Simulation

To test the implementation of the wide-range model for the permittivity in IMD, simulations in IMD and Polly-2T were run using the same starting parameters as in [4]. The IMD simulations used the wide-range model implementation for ϵ, while Polly-2T had its wide-range model for the electron thermal conductivity and electron-phonon coupling deactivated. The IMD simulations had to be run on one CPU, due to the limitations of the new energy allocation scheme (see Sec.6.3.4). This increased the simulation time to 2.5 weeks but would counteract another bug in IMD where large fluences would lead to atoms jumping CPUs. The bug in the TTM still persisted in these simulations. The absorbed fluences in IMD and Polly-2T are then calculated using (5.1) and (6.1).

6.3.6 Data Analysis

The absorbed fluences Φ_{abs} for IMD and Polly-2T can be found in Tab. 6.2. The data in this table shows that IMD with the wide-range model for the permittivity follows a similar behaviour as Polly-2T. By increasing the pulse duration the absorbed energy is increased. This only occurs because the permittivity and therefore the reflectivity and absorption coefficient in IMD are now calculated using the wide-range model. Since a longer pulse duration leaves the system more time to react to the already absorbed energy, the increased absorption coefficient and reduced reflectivity lead to a larger total absorbed energy.
However, comparable results only exist for low fluences and low pulse durations, as higher fluences and thus higher absorbed energies trigger the bug in IMD's two temperature model. This becomes obvious in Fig. 6.9, where the IMD results deviate further from Polly-2T with increasing surface fluences and pulse duration. Especially for 5 ps the IMD results vary vastly from Polly-2T due to the bug affecting the energy for a longer duration than for shorter pulses. From Tab. 6.2 we can see that for fluences of 1.49 and 2.97 J/cm^2 and a pulse length of 5 ps

Table 6.2: Simulation parameters for testing the implementation of the wide-range model for the electric permittivity in IMD. Characterizing starting parameters for IMD and Polly-2T, surface fluence and pulse duration, taken from [4]. *due to the bug in the TTM, these values were calculated by using the peak energy gain within the 10 σ_t range of the pulse maximum.

Surface Fluence Φ_{surf}	**Pulse duration τ**	$\Phi_{abs,IMD}$*	$\Phi_{abs,Polly\text{-}2T}$
[J/cm^2]	[fs]	[J/cm^2]	[J/cm^2]
0.19	50	0.011	0.013
0.37	50	0.026	0.032
0.74	50	0.074	0.089
1.49	50	0.288	0.270
2.97	50	0.937	0.795
0.19	500	0.014	0.016
0.37	500	0.034	0.039
0.74	500	0.107	0.100
1.49	500	0.375	0.265
2.97	500	1.057	0.693
0.19	5000	0.024	0.018
0.37	5000	0.133	0.047
0.74	5000	0.666	0.173
1.49	5000	2.315	0.526
2.97	5000	6.205	1.189

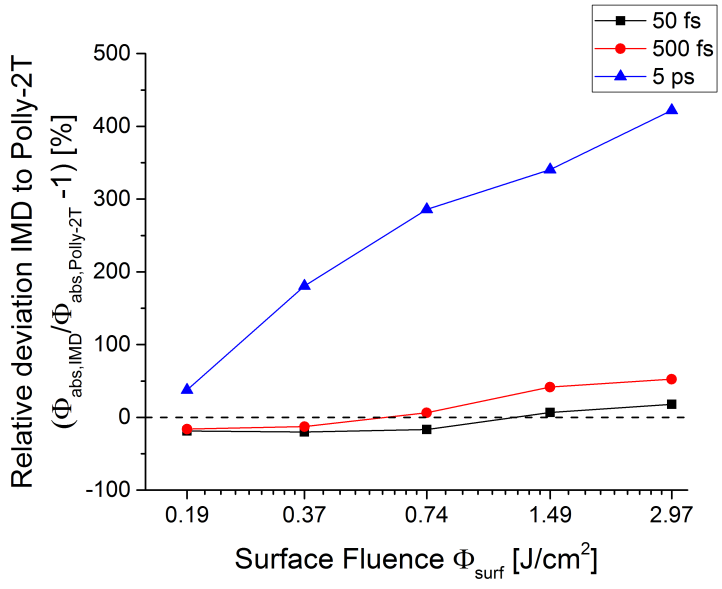

Figure 6.9: Relative deviations of the IMD simulations from Polly-2T.

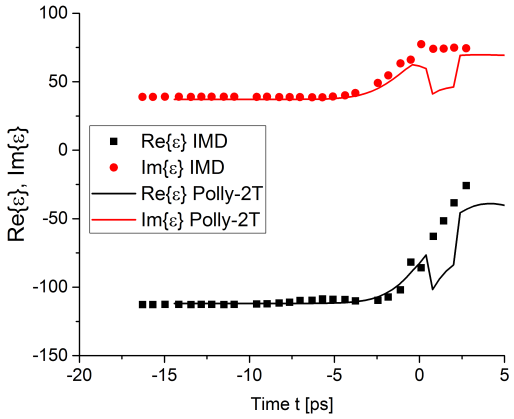

(a) $\Phi_{surf} = 0.19$ J/cm^2

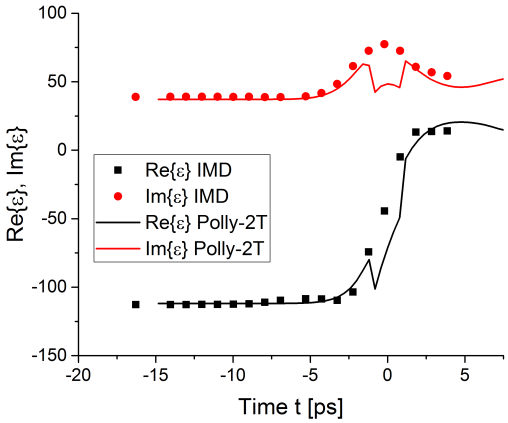

(b) $\Phi_{surf} = 0.37$ J/cm^2

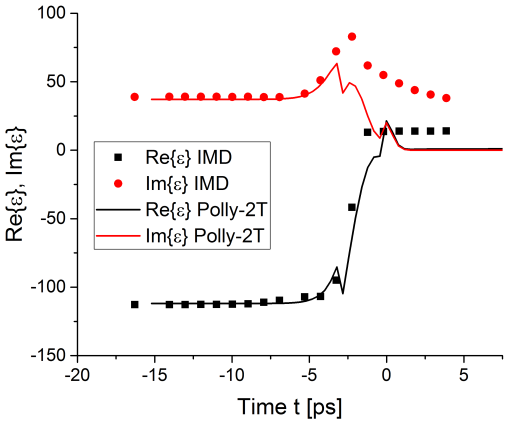

(c) $\Phi_{surf} = 1.49$ J/cm^2

Figure 6.10: Evolution of the complex permittivity on the surface of the target in IMD and Polly-2T. Simulations used a pulse length of $\tau = 5$ ps.

the absorbed fluence exceeds the incident fluence thus showing the influence of the bug in the two temperature model.

More precise information about the validity of the wide-range model in IMD can be acquired by comparing the permittivity data generated with the two codes. This is achieved by comparing the temporal evolution of the permittivity on the surface of the target. However, the permittivity data from Polly-2T is rather limited, since the output files contain only permittivity data from within the $10\sigma_t$ range of the pulse maximum. Since Polly-2T simulations with $\tau = 50$ and 500 fs will only contain data for three different time steps, these data sets are no useful basis for a comparison. Hence the permittivity data for simulations with $\tau = 5$ ps is compared. The first observation from Fig. 6.10 is that IMD and Polly-2T produce the same results for material at room temperature during the starting phase of the simulation. Figures 6.10(a) and 6.10(b) also show a good agreement between IMD and Polly-2T for the rising flank of the permittivity except for the temporary drop in the Polly-2T curve. This drop must be caused by a different behaviour of one or more arguments in the TTM, i.e. the thermal energy of the electrons T_e, the

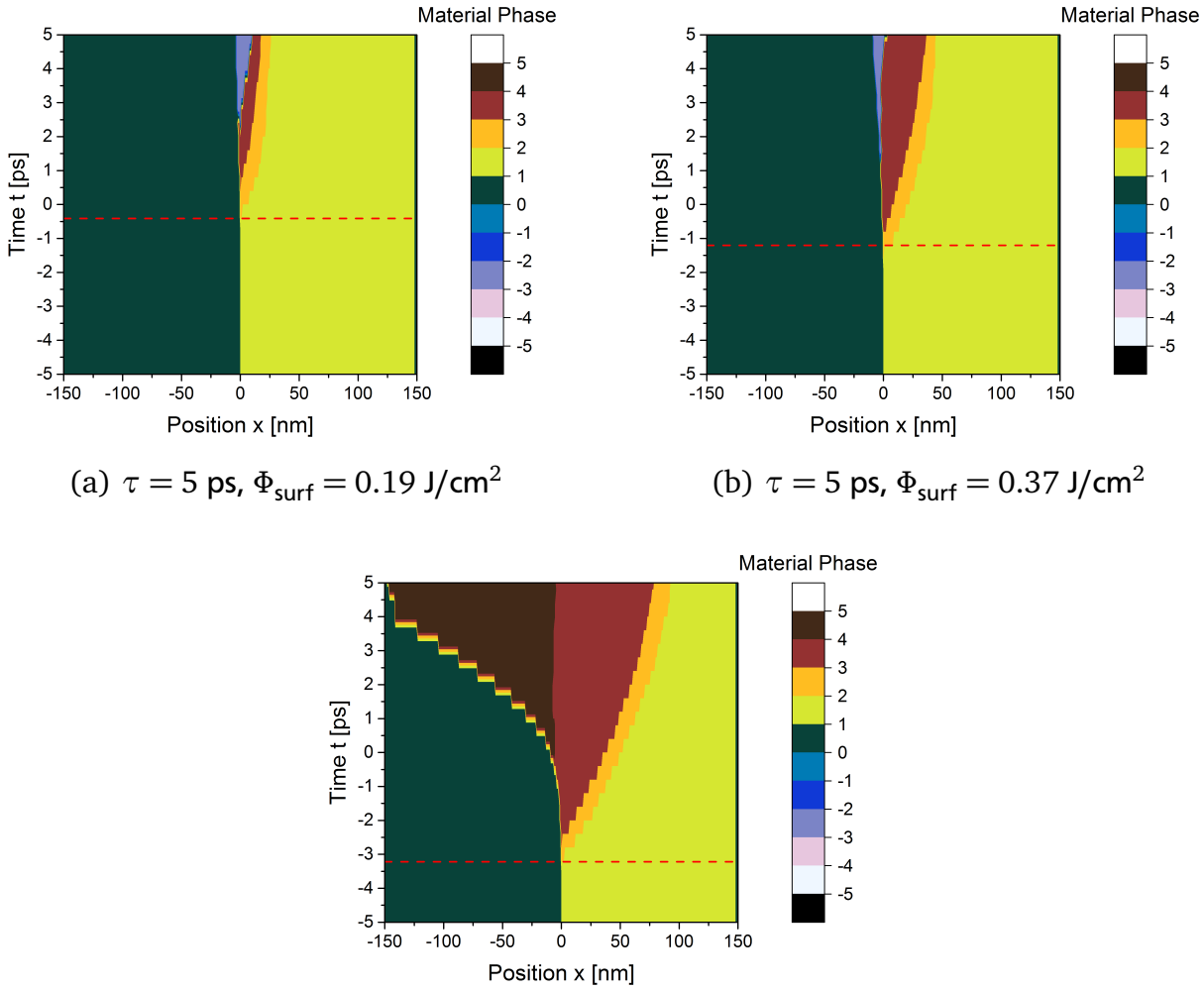

(a) $\tau = 5$ ps, $\Phi_{surf} = 0.19$ J/cm^2

(b) $\tau = 5$ ps, $\Phi_{surf} = 0.37$ J/cm^2

(c) $\tau = 5$ ps, $\Phi_{surf} = 1.49$ J/cm^2

Figure 6.11: Temporal and spacial distribution of material phases in Polly-2T. The dashed line denotes the time at which the permittivity in Fig. 6.10 drops. (0 = vacuum, 1 = solid, 2 = liquid-solid, 3 = liquid, 4 = liquid-gas, 5 = gas, -1 = metastable solid, -2 = metastable liquid-solid, -3 = metastable liquid, -4 = metastable liquid-gas, -5 = metastable gas)

temperature of the lattice T_i or the density ρ. The laser wavelength can be excluded as a possible cause, since both codes treat the wavelength as fixed. Since the drop occurs rather rapidly, the cause must be a non-linear effect such as ablation of a material layer or a phase transition that has a different implementation in Polly-2T than in IMD. This assumption is supported by Fig. 6.11, which shows that the rapid decay in the permittivity coincides with a phase transition from the solid state into a mixed solid and liquid state. Since this phase transition causes the density ρ of aluminium to drop the permittivity is affected accordingly.
A comparison between the different surface fluences in Fig. 6.10 shows that for small fluences IMD and Polly-2T produce comparable results for the permittivity, while Fig. 6.10(c) shows an increasing discrepancy between the imaginary part of ϵ in IMD and Polly-2T for higher fluences. This is most likely caused by the bug in the two temperature model, where the thermal energy of the electrons shows an unphysical increase. Since T_e is an argument of the wide-range model the result of the permittivity will therefore be affected by the increased energy.

6.3.7 Conclusion

Figure 6.10 shows that for low fluences the newly implemented wide-range model in IMD produces similar permittivity values as Polly-2T. Deviations caused by rapid changes in the data from Polly-2T simulations can be linked to phase transitions. IMD seems to either lack a proper implementation of phase transitions or utilizes a different calculation scheme with different results. Comparability is reduced for higher fluences, since the unphysical behaviour of the electron thermal energy discussed in chapter 5 directly influences the input parameters of the wide-range model.
Since results for room temperature and low fluences are comparable under certain constraints the implementation of the wide-range model for the electric permittivity is considered to be successful. Though it would be prudent to test this implementation after a fix for the TTM bug has been applied.

6.4 Wide-range model for κ_e and γ_{ei} in IMD

The wide-range model for the electron thermal conductivity κ_e and the electron-phonon coupling coefficient γ_{ei} is based on equations (3.13) - (3.20). The implementation for κ_e was done parallel to the wide-range model of the permittivity, while the implementation for γ_{ei} occurred during the last simulation runs.

6.4.1 Implementation

Since the wide-range model discussed in [11] contains similar parts for the permittivity, the electron thermal conductivity and the electron-phonon coupling, the implementation of these functions for κ_e and γ_{ei} is based on the implementation for ϵ. Most support functions needed for the calculation of the permittivity could also be used to calculate the conductivity and coupling. The implementation of the electron thermal conductivity included the functions to calculate the contributions in the metallic and plasma phase and the interpolation between these states. Further was the constructor of the TTM-elements enhanced to allocate a κ_e to each cell. The static implementation of the electron thermal conductivity was then replaced by reading the dynamic κ_e from the affected cell. The TTM output files were altered to additionally contain the electron thermal conductivity of each cell. A switch in the parameter file called *fd_WR* allows for switching between a constant electron thermal conductivity and the wide-range calculation. To implement the wide-range model for electron-phonon coupling a debugging function of the original IMD code had to be disabled since it would interfere with the change from a constant global coupling coefficient to a time and location dependent one. Again the constructor for the TTM-elements was modified to store the coupling coefficient of the cell. Equation (3.19) was implemented and the output file altered to contain the coupling coefficient for every cell. The wide-range calculation was then implemented to replace the constant γ_{ei}. The upgrade was then linked to the *fd_WR* parameter to switch between constant or dynamic calculation of the transport properties κ_e and γ_{ei}.

6.4.2 Simulation

The simulations for this upgrade step used only the wide-range model for the thermal conductivity since the upgrade of the electron-phonon coupling was still exhibiting bugs. These bugs would lead to a freeze of the simulation after the first simulation step and time constraints prevented the development of a solution for this problem. The simulations used the same parameter sets as in Ch.6.3.5 but with *fd_WR* enabled. The corresponding Polly-2T simulations used only the downgrade for a fixed electron-phonon coupling coefficient.

6.4.3 Data Analysis

Since Polly-2T has no output file containing the distribution of the electron thermal conductivity, the analysis of this upgrade is limited to the analysis of the absorbed fluence. Fig. 6.12 shows the relative deviation of the absorbed fluence in IMD compared to the absorbed fluence in Polly-2T. From the data we see that for pulse lengths of $\tau = 50$ and 500 fs the absorbed fluences in

Table 6.3: Simulation parameters for testing the implementation of the wide-range model for the electron thermal conductivity in IMD. Characterizing starting parameters for IMD and Polly-2T, surface fluence and pulse duration, taken from [4]. *due to the bug in the TTM, these values were calculated by using the peak energy gain within the 10 σ_t range of the pulse maximum.

Surface Fluence Φ_{surf}	Pulse duration τ	$\Phi_{abs,IMD}$*	$\Phi_{abs,Polly\text{-}2T}$
[J/cm^2]	[fs]	[J/cm^2]	[J/cm^2]
0.19	50	0.004	0.013
0.37	50	0.009	0.029
0.74	50	0.023	0.079
1.49	50	0.075	0.255
2.97	50	0.471	0.770
0.19	500	0.005	0.015
0.37	500	0.010	0.034
0.74	500	0.027	0.085
1.49	500	0.095	0.233
2.97	500	0.386	0.647
0.19	5000	0.012	0.017
0.37	5000	0.047	0.039
0.74	5000	0.259	0.129
1.49	5000	1.081	0.449
2.97	5000	2.370	1.134

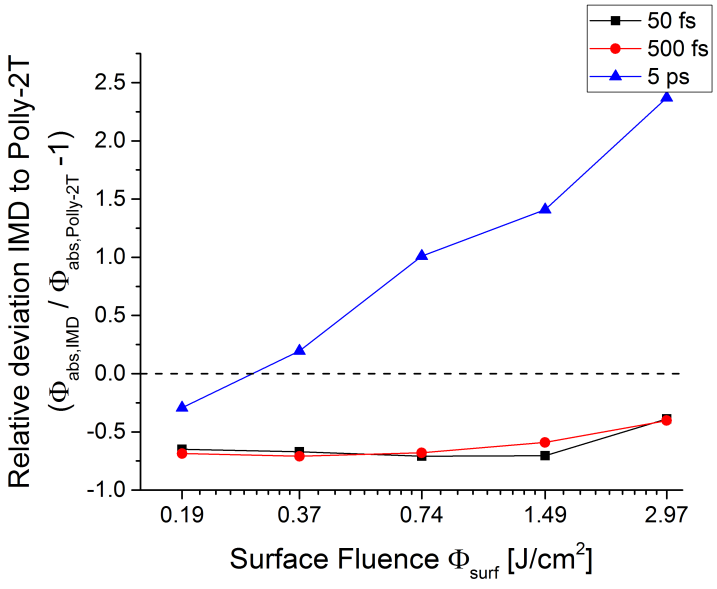

Figure 6.12: Relative deviations of the IMD simulations from Polly-2T.

IMD with dynamic electron thermal conductivity are far lower than the results of Polly-2T. For a pulse length of $\tau = 5$ ps and low fluences IMD also absorbs far less fluence than Polly-2T. This changes for higher fluences as the absorbed fluences in IMD rise faster than in Polly-2T and almost exceed the incident fluence.

6.4.4 Conclusion

Considering the bug in the two temperature model for higher fluences a valid comparison of the absorbed fluences is only possible for surface fluences of $\Phi_{\text{surf}} = 0.19$ and 0.37 J/cm^2. This upgrade shows a considerable discrepancy between the absorbed fluence in IMD and Polly-2T for all fluences. thus leading to the conclusion that these This leads to the conclusion that either a bug exists in the implementation of the wide-range model of the electron thermal conductivity or the discrepancies are caused by the interactions of both wide-range models with the TTM bug in the thermal energy of the electrons. A further study of the problems with the implementation of κ_e and γ_{ei} and possible fixes was prevented due to time constraints.

7 Discussion

To validate the usefulness of the complete upgrade a comparison between the different steps presented in Ch.6 is necessary. Fig. 7.1 shows the relative deviations ($\frac{\Phi_{\text{abs,IMD}}}{\Phi_{\text{abs,Polly-2T}}} - 1$) of the absorbed fluences in IMD compared to the ones in Polly-2T. The cold reflectivity and dynamic reflectivity step are both represented by a single data point. During the cold reflectivity upgrade the focus was on the angular behaviour of the simulation and not the incident fluence and the pulse length. Similarly, the dynamic reflectivity step was geared towards testing if the IMD code would still produce viable results while using a time-dependent reflectivity instead of a fixed one. This variable reflectivity leads to a higher absorbed fluence in the dynamic reflectivity simulation. From ch.5 we would expect the deviations to increase due to the increased energy absorption triggering the TTM bug. However, Fig. 7.1 shows that the deviation to Polly-2T decreases while using the dynamic reflectivity upgrade. For the first and second upgrade step we see that the absorbed fluence in IMD is larger than the one in Polly-2T.
The implementation of the wide-range model for the permittivity in IMD changes this behaviour for lower fluences. The absorbed fluences in IMD are now lower for surface fluences below 0.74 J/cm^2 yet the magnitude of the deviation is further reduced. For higher fluences and pulse durations the bug in the two temperature model increasingly dominates the absorbed energy, since the wide-range model and the absorption process are linked by thermal energy of the electrons. A comparison between the implementation of the wide-range permittivity with the implementation of wide-range ϵ and wide-range κ_e shows that far less energy is absorbed in the system. The simulations with WR ϵ feature a decreasing reflectivity during runtime due to the changes in the permittivity. This leads to more energy being absorbed in the material. Since the thermal conductivity is kept fix in these simulations the increased temperature in the surface dissipates by the same amount however high T_e might be. In the simulations with the additional implementation of the wide-range thermal conductivity for the electrons the thermal conductivity is increased with increasing electron temperature. Thus more energy is dissipated from the surface than with fixed κ_e. This leads to T_e in the surface being reduced and therefore the reflectivity drops not as steep as with a fixed thermal conductivity. The result is a lower absorbed energy for simulations employing the wide-range model for the electron thermal conductivity. From Fig. 7.1 we see that the deviations from Polly-2T are especially large for this upgrade step, leading to the conclusion that further studies of the implementation and effect of the wide-range electron thermal conductivity are necessary.

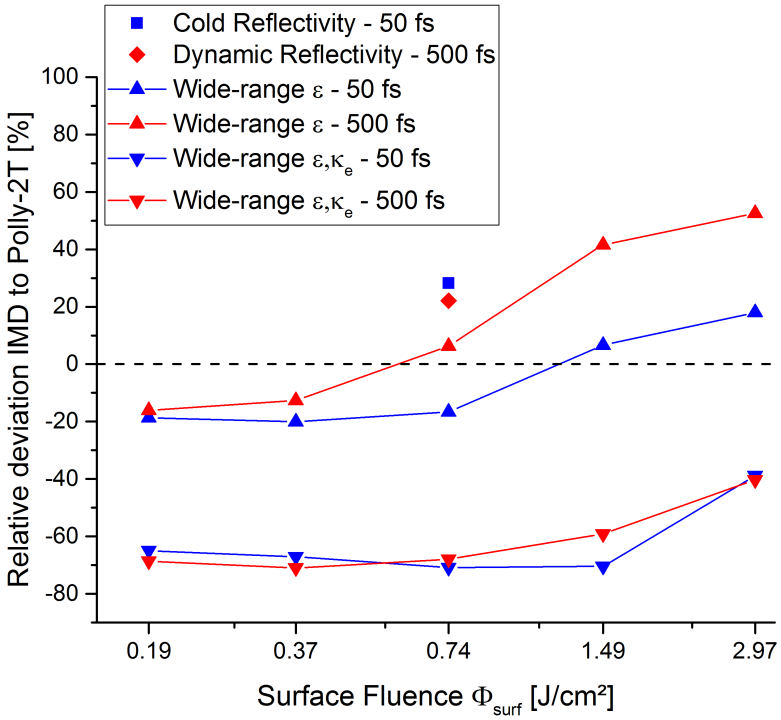

Figure 7.1: Relative deviation ($\frac{\Phi_{abs,IMD}}{\Phi_{abs,Polly\text{-}2T}} - 1$) of the absorbed fluence Φ_{abs} in IMD and Polly-2T. In every IMD upgrade step Polly-2T used the appropriate downgrade step to serve as a benchmark.

The idea behind this thesis was to gain a tool for simulating the laser ablation process in metals and to apply this knowledge to the concept of laser-ablative micro-thrusters. These micro-thrusters can be characterized by their specific impulse I_{sp} and momentum coupling coefficient c_m. From the data gained in Ch.6.3.5 we can calculate I_{sp} and c_m for the simulation of the ablation process. Fig. 7.2(a) shows the specific impulse calculated with IMD and Polly-2T while using the wide-range model for the permittivity, constant thermal conductivity and constant electron-phonon coupling. We see that for low fluences IMD and Polly-2T achieve almost the same I_{sp} yet for higher fluences the specific impulse rises faster in Polly-2T then in IMD. This is plausible for lower surface fluences as Fig. 7.1 shows that for fluences of $\Phi_{surf} < 0.74$ J/cm^2 the absorbed energy in IMD is lower than in Polly-2T. However, for fluences $\Phi_{surf} > 0.74$ J/cm^2 the absorbed energy in IMD exceeds the one in Polly-2T, yet the specific impulse does not. A possible explanation for this behaviour might be that higher fluences trigger different phase transitions in the surface layer of Polly-2T simulations. This leads to vapor ejection for higher fluences that contains particles with higher velocities than the solid or liquid material ejected at lower fluences. Fig. 6.10 showed that the process of phase transitions is different in IMD and Polly-2T.

Fig. 7.2(b) shows the momentum coupling coefficient for the same simulations. From the data we can see that the momentum coupling in the plume in IMD is radically different from the behaviour in Polly-2T. This however can not be explained by reaching different ablation regimes, since Fig. 5 b) in [16] shows that different ablation regimes still result in momentum coupling coefficients of similar magnitude.

Fig. 7.2 shows a comparison between the specific impulse and the momentum coupling obtained with the original IMD and Polly-2T(VLL) and the upgraded IMD code and Polly-2T with constant κ_e and γ_{ei}. In Fig. 7.2(a) we see that the I_{sp} values from [4] are always lower than the results obtained with the modified versions. We also see that the original versions had a good agreement for $\Phi_{surf} = 0.37$ J/cm^2 and 0.74 J/cm^2 while the modified versions of IMD and Polly-2T have a fairly good agreement for fluences lower than 0.74 J/cm^2.

The different behaviour of the modified Polly-2T code to the original Polly-2T is most probably caused by the electron thermal conductivity and the electron-phonon coupling being fixed since these are the only differences in the simulations. In the wide-range model these parameters would increase the energy transport from the electron system into the lattice as well as the energy transport from one cell into its neighbouring cells. Since this is blocked by κ_e and γ_{ei} being fixed, the energy in the electron system of a certain cell is going to build up.

In IMD the differences might be caused by the much lower penetration depth of the laser due to the wide-range model for the permittivity. This leads to a higher temperature in the surface layers where the ablation occurs and thus higher kinetic energies and therefore higher I_{sp}. This higher temperature in the surface layer might also be the cause of the large deviations shown in Fig. 7.2(b) for the upgraded IMD code compared to the original IMD version.

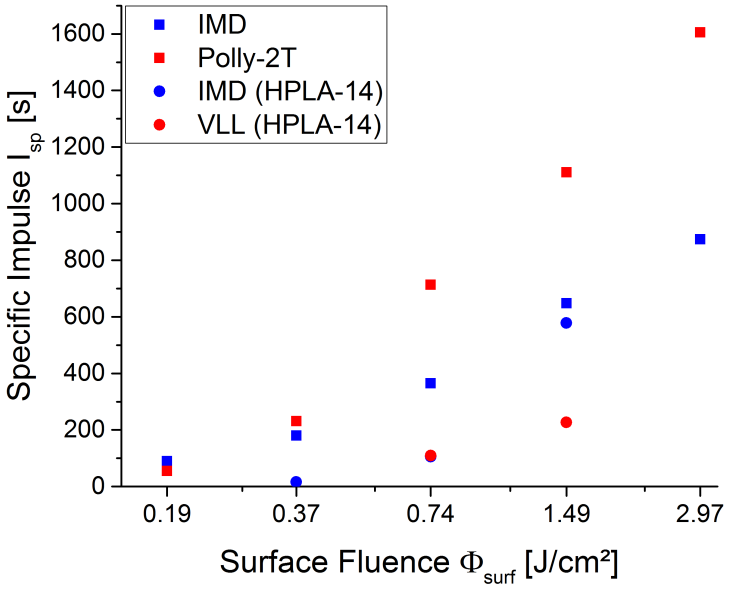

(a)

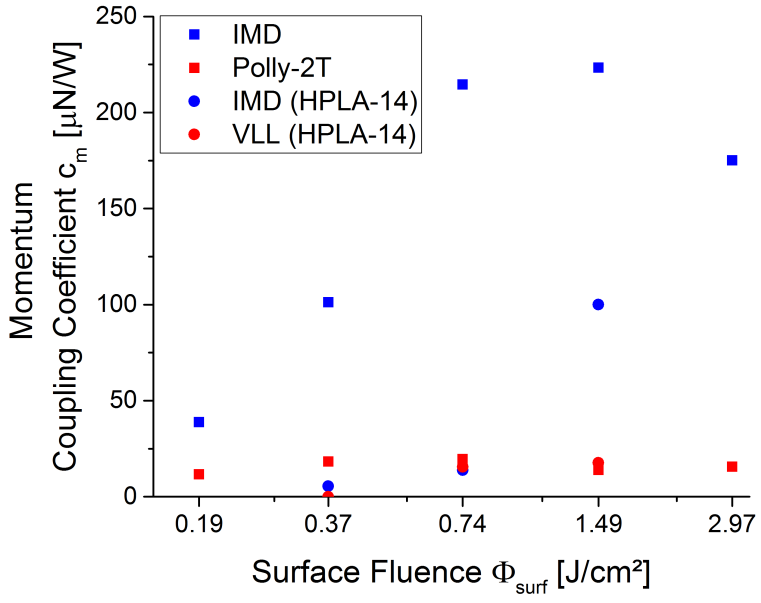

(b)

Figure 7.2: Comparison between the IMD and Polly-2T code with the wide-range model for ϵ and fixed κ_e,γ_{ei} and the simulations from [4]. $\tau = 500$ fs

8 Summary and Outlook

Upgrades to the IMD source code enabled the software tool to autonomously calculate the absorbed energy. This is achieved by utilizing the Fresnel equations to calculate the losses due to reflection and a wide-range model to calculate the dynamic refraction index and absorption coefficient. All three primary upgrade steps of the IMD code can be activated through the parameter file. The wide-range calculation of the thermal conductivity of the electrons and the electron-phonon coupling can be activated independently.
The first upgrade step does have no further use, since it is completely implemented in the third step. The second upgrade step might be useful for running semi-empirical simulations with reflectivity evolutions acquired from experiments.
The comparison with Polly-2T showed that for low fluences and short pulse durations the results are similar, yet higher fluences and pulse durations lead to larger discrepancies. This can be attributed to a bug in the two temperature model in IMD. A fix for this bug is already in development but was not available as of the end of this thesis. Further the newly implemented energy absorption scheme in IMD requires an upgrade to re-enable the parallel processing capability of IMD, which was not possible to implement due to time constraints. It would also be prudent to revise the energy allocation such that ablated material can also be heated. This might be irrelevant for short pulses where the pulse is finished before material is ablated yet for longer pulses material heating and intensity shielding in the plume are required. This would be possible by implementing the beam in wave optics and solving the Helmholtz-Equations for each cell, similar to the process in Polly-2T. Since the optional goal for upgrading the electron-phonon coupling is still suffering from bugs a fix would also be a possible future task.

9 Acknowledgement

Thanks for the support given during the work presented here go to Dr. Stefan Scharring of the Institute of Technical Physics (DLR) for his knowledge and support regarding the visualisation and interpretation of the simulation data as well as his support in general, PD Dr. Johannes Roth of the Institute for Functional Quantum Matter from the University of Stuttgart for his support and inside knowledge of the IMD code and Dr. Mikhail Povarnitsyn of the Joint Institute for High Temperatures at the Russian Academy of Sciences for kindly providing us with the Polly-2T source code. Last but not least, I would like to thank Dr. Hans-Albert Eckel, Professor Dr. Markus Roth and PD Dr. Adolf Giesen for enabling this project.

Bibliography

[1] NASA. http://lisa.nasa.gov, June 2011. Accessed 02.19.2015.

[2] H.-A. Eckel et al. Overview of Laser Ablation Micropropulsion Research Activities at DLR Stuttgart. In *HPLA/BEP 2014*, April 2014. Conference CD, http://elib.dlr.de/89091/.

[3] S. Scharring. Vorlesung Laserantriebe at the Instituite of Space Systems, University of Stuttgart, June 2014. Lecture during summer semester.

[4] S. Scharring et al. Open Access Tools for the Simulation of Ultrashort-Pulse Laser Ablation. In *HPLA/BEP 2014*, April 2014. Conference CD, http://elib.dlr.de/89090/.

[5] F. Träger, editor. *Handbook of Lasers and Optics*. Springer Science+Business Media, LLC New York, 2007.

[6] D. Bäuerle. *Laser Processing and Chemistry*. Springer, Berlin, 3rd edition, 2000.

[7] S.I. Anisimov et al. Electron emission from metal surfaces exposed to ultrashort laser pulses. *Sov.Phys.-JETP*, 39(2):375–377, August 1974.

[8] IMD The ITAP Molecular Dynamics Program. http://imd.itap.physik.uni-stuttgart.de/index.html. Accessed 02.20.2015.

[9] J. Roth. IMD - a molecular dynamics program and applications. In J. Grotendorst R. Esser, P. Grassberger and M. Lawerenz, editors, *Proceedings of the Workshop on Molecular Dynamics on Parallel Computers*, page 83, Singapore, 2000. World Scientific.

[10] F. Ercolessi and J. B. Adams. Interatomic potentials from first-principles calculations: The force-matching method. *EPL (Europhysics Letters)*, 26:583, 1994.

[11] M. E. Povarnitsyn et al. A wide-range model for simulation of pump-probe experiments with metals. *Applied Surface Science*, 258:9480, July 2012.

[12] D. Förster. Validation of the software package IMD for molecular dynamics simulations of laser induced ablation for micro propulsion. Master's thesis, University of Stuttgart, June 2013.

[13] M. E. Povarnitsyn et al. Dynamics of thin metal foils irradiated by moderate-contrast high-intensity laser beams. *Physics of Plasmas*, 19(2)(023110-1), 2012.

[14] S. Scharring. Review on Laser Lightcraft Research. In *HPLA/BEP 2014*, April 2014. Conference CD, http://elib.dlr.de/89089/.

[15] J. Cheng et al. Effects of laser operating parameters on metals micromachining with ultrafast lasers. *Applied Surface Science*, 256(1514), 2009.

[16] S. Scharring et al. Low-Noise Thrust Generation by Laser-Ablative Micropropulsion. In *Joint Conference of 30th ISTS*, July 2015.

10 Appendix

IMD Units

Table 10.1: Table of IMD units as shown in [12]

Quantity	**Definition**	**IMDu ↔ SI**
energy E		$1\ \text{eV} = 1.60217733 \cdot 10^{-19}\ \text{J}$
distance x		$1\ \text{Å} = 10^{-10}\ \text{m}$
mass m		$1\ \text{amu} = 1.660538 \cdot 10^{-27}\ \text{kg}$
time t	$[t] = \sqrt{\frac{[m][x]^2}{[E]}}$	$1\ \text{IMDu(t)} = 10.1806 \cdot 10^{-15}\ \text{s}$
temperature T	$[T] = \frac{3}{2}\frac{[E]}{[k_B]}$	$1\ \frac{eV}{k_B} = 1.60217733 \cdot 10^{-19}\ \frac{J}{k_B} \approx 11,605\ \text{K}$
pressure p	$[p = \frac{[m]}{[x][t^2]}]$	$1\ \text{IMDu}(p) \approx 1.60222 \cdot 10^{11}\ \text{Pa}$
electron-phonon coupling parameter G	$[G] = \frac{[E]}{[t][x^3][T]}$	$1\ \text{IMDu(G)} \approx 1.3561 \cdot 10^{21}\ \frac{J}{sm^3K}$
heat capacity C	$[C] = \frac{[E]}{[x^3][T]}$	$1\ \text{IMDu(C)} \approx 1.3806 \cdot 10^{7}\ \frac{J}{m^3K}$
thermal conductivity K	$[K] = \frac{[E]}{[x][t][T]}$	$1\ \text{IMDu(K)} \approx 13.561\ \frac{J}{smK}$
proportional coefficient γ	$[\gamma] = \frac{[C]}{[T]}$	$1\ \text{IMDu}(\gamma) \approx 1,189.7\ \frac{J}{m^3K^2}$
fluence Φ	$[\Phi] = \frac{[E]}{[x^2]}$	$1\ \frac{eV}{Å^2} \approx 16.022\ \frac{J}{m^2}$

Software Modifications

The source code containing the modifications for the IMD upgrade and the Polly-2T downgrade can be found in the complementary disc of this thesis.

Simulation Graphics

The full set of graphics generated from the simulations for this thesis can also be found on the disc.